

SCATTERING OF ARGON AND NITROGEN
OFF POLYCRYSTALLINE NICKEL

by
R. G. Wilmoth
and
O. F. Hagena

Technical Report
National Aeronautics and Space Administration
Grant No. NGR 47-005-046

Division of Aerospace Engineering and Engineering Physics
RESEARCH LABORATORIES FOR THE ENGINEERING SCIENCES
SCHOOL OF ENGINEERING AND APPLIED SCIENCE
UNIVERSITY OF VIRGINIA
CHARLOTTESVILLE, VIRGINIA

Report No. AEEP-4038-105-67U
August 1967

Copy No. 4

PRECEDING PAGE BLANK NOT FILMED.

FOREWORD

This report is the master's thesis of Mr. Wilmoth. His principal adviser in this effort was Dr. Hagen. This research was carried out under NASA Grant NGR 47-005-046 as a part of an investigation into molecular collision phenomena, using molecular beam techniques under the direction of S. S. Fisher, O. F. Hagen, A. R. Kuhlthau, J. E. Scott, Jr. and R. N. Zapata.

ABSTRACT

An aerodynamic molecular beam has been used together with a sensitive time-of-flight detection system to measure the distribution of flux and speeds of thermal-energy particles scattered from polycrystalline nickel surfaces. At room temperature, the distribution of reflected flux varies much as the cosine of the angle of reflection. Highly lobular flux distributions were observed after prolonged heating of the surface in a vacuum. Time-of-flight measurements indicate the following for the speeds of the scattered particles:

1. Thermal accommodation shows a strong dependence on the angle of reflection.
2. The thermal spread is in general smaller than that of an effusive Maxwellian distribution at the surface temperature and is always larger than the spread in the incident velocities.

An analysis of a method of fitting analytic expressions to the measured time-of-flight curves indicates that such a method provides a reasonably accurate means of obtaining the average speed and energy of the reflected particles.

TABLE OF CONTENTS

	<u>PAGE</u>
FOREWARD	iii
ABSTRACT	v
LIST OF FIGURES	xi
LIST OF SYMBOLS	xiii
SECTION I INTRODUCTION	1
SECTION II EXPERIMENTAL APPARATUS	4
2.1 INTRODUCTION	4
2.2 VACUUM SYSTEM	4
2.3 BEAM SOURCE	6
2.4 TARGET	6
2.5 TOF METHOD	10
Chopper	10
Detector	11
SECTION III DATA REDUCTION	13
3.1 PARAMETERS OF THE TOF CURVE	13
TOF at Maximum Signal	13
TOF at Half-Maximum Signal	15
Determination of Flux	15
3.2 MOMENTS OF THE TOF CURVE	16
Numerical Integration	16
Moments from Fitted Curve	18
SECTION IV EXPERIMENTAL RESULTS	20
4.1 "DIRTY" ROOM TEMPERATURE TARGET	20
Flux Distribution	20
TOF Distribution	22

	<u>PAGE</u>
4.2 EFFECT OF SURFACE TEMPERATURE AND TEMPERATURE HISTORY	24
Effect of Temperature History at Fixed θ_r	25
Effect of Heat Treatment on Reflected Spectrum	28
(a) "Dirty" Target	28
(b) "Clean" Target	30
4.3 EFFECTS OF ANGLE OF INCIDENCE AND BEAM GAS MOLECULAR WEIGHT	32
Angle of Incidence	32
Beam Gas Molecular Weight	34
4.4 MODIFYING INFLUENCES ON THE DATA	34
Effect of Resolution	34
Changes in Incident Beam Flux	35
Changes in Background Pressure	35
4.5 REPEATABILITY	36
SECTION V COMPARISON TO VARIOUS MODELS	38
5.1 DIFFUSE REFLECTION MODEL	38
5.2 SPECULAR REFLECTION	40
5.3 HARD-CUBE MODEL	41
5.4 ADDITIONAL MODELS	44
Nocilla's Re-emission Law	44
Hinchen and Shepherd	45
"Rough-Surface" Model	46
Other Models	46
SECTION VI SUMMARY AND CONCLUSIONS	47
BIBLIOGRAPHY	50
APPENDIX - CURVE-FITTING VS. NUMERICAL INTEGRATION	54
A.1 DERIVATION OF MOMENTS FROM FITTED CURVE	55

	<u>PAGE</u>
A.2 APPLICATION TO SAMPLE SET OF DATA	58
A.3 EFFECT OF RESOLUTION	63

LIST OF FIGURES

	<u>PAGE</u>
Figure 2.2.1 Experimental Setup for Time-of-Flight Experiments of Direct and Reflected Molecular Beams	5
Figure 2.4.1 Target and Holder	7
Figure 3.1.1 Sample Recording of TOF Distributions . .	14
Figure 4.1.1 Flux Distributions for Argon and Nitrogen Beams Scattered from a Room Tempera- ture Target	21
Figure 4.1.2 Comparison of Measured Reflected Beam TOF Signals with that Predicted for Maxwellian Effusion with Full Thermal Accommodation	23
Figure 4.2.1 Time History for Scattered Nitrogen Beam Signal Height with Target Temperature Variation, $\theta_i = \theta_r = 60^\circ$, Nitrogen Beam Gas	26
Figure 4.2.2 Variation of I/I_o , t_m/t_i , and $t_m/\Delta t$ with Scattering Angle: Nitrogen Beam, $\theta_i = 60^\circ$	29
Figure 4.3.1 Effect of Angle of Incidence and Beam Gas on I/I_o , t_m/t_i , and $t_m/\Delta t$	33
Figure A.1 Working Curves for \bar{v} and $\sqrt{v^2}$	59
Figure A.2 TOF Distributions for Nitrogen Scattered from Hot Nickel	60
Figure A.3 Comparison of Measured and Fitted TOF Distributions	61
Figure A.4 Comparison of Moments by Numerical Integration and by Curve-Fit Method	62
Figure A.5 Effect of Resolution on \bar{v} and $\sqrt{v^2}$	65

LIST OF SYMBOLS

a	Ratio of time-of-flight at maximum signal, t_m , to time-of-flight at half maximum, t_1 or t_2
A, A'	Constants in the distribution function
B	$= \beta L$
E	Energy
$g(a)$	Function of a , defined in Appendix
$h(a)$	Function of a , defined in Appendix
i^-	Electron current
i^+	Ion current
I	Scattered beam flux (particles/cm ² sec or particles/sterad. sec.)
I_0	Scattered beam flux normal to "dirty" target
k	Boltzmann constant
l_{eff}	Effective electron path length in TOF detector
L	Length of flight path (distance from chopper disc to active zone of detector)
m	Molecular mass
n	Fitting exponent
n	Particle density
R	Resolution = $\Delta t / T$
R_L	Input resistor of preamplifier
S	Speed ratio = $v_0 / \sqrt{2kT_e/m_g}$
S	Fitting parameter
$S_d(t)$	Detector signal (or TOF distribution)

t	time
t_m	Time-of-flight at maximum detector signal
t_1, t_2	Time-of-flight at half-maximum detector signal
t_o	$= L/v_o$
t^*	$= \beta_s L/\sqrt{2}$
T	Temperature ($^{\circ}\text{K}$)
TOF	Time-of-flight
v	Particle speed
v_o	Streaming speed
\bar{v}, \bar{v}^2	Mean speed and mean square speed, respectively
α	Thermal accommodation coefficient
β	Fitting parameter
β_s	$= \sqrt{m_g/2kT_s}$
Δt	Half-width of detector signal ($= t_2 - t_1$)
θ_i	Angle of incidence measured from target normal
θ_r	Angle of reflection measured from target normal
μ	Mass ratio $= m_g/m_s$
σ_{eff}	Effective ionization cross-section
τ	Effective chopper opening time

SUBSCRIPTS

e	Flow value
i	Incident beam
r	Reflected beam
s	Surface
o	Quantities in unchopped beam or for infinite resolution

SECTION I

INTRODUCTION

Gas-surface interactions have been the subject of an extensive amount of experimental and theoretical study. The results find practical application in such areas as adsorption processes, catalysis, and aerodynamic drag and heat transfer in rarefied gas flows. The problem is concerned with the fundamentals of the energy and momentum exchange during intermolecular collisions. Difficulties arise in both the theoretical and experimental studies in that one is forced to consider the microscopic details of a many-body, statistical problem. Several models have been suggested to explain the observed experimental phenomena; however, no single model is able to predict all of the experimental results. Until a sufficient understanding of the interaction mechanism exists, the details of the scattering process must continue to be studied experimentally.

Molecular beams produced from effusive sources have provided a useful research tool in the study of gas-surface interactions, and summaries of some of the experimental work may be found in references (1) and (2). However, effusive (or oven) beams are somewhat limited in incident beam flux, and this limitation results in difficulties in detection due to the

attenuation of the flux in the scattering process. Development of the nozzle-type molecular beam has overcome the problem of low incident flux, and in addition, a highly collimated, more nearly monoenergetic beam is produced⁽³⁾. This is desirable, because the details of the scattering process tend to be obscured for a large spread in incident velocities. An initial study, using such a nozzle-type beam scattered from engineering surfaces, has been reported by Kuhlthau and Bishara⁽²¹⁾.

Most of the experiments mentioned in references (1) and (2) have reported measurements of only the angular distribution of scattered particles. It has been generally assumed that the velocity distribution of the scattered particles would be nearly that corresponding to effusion from the surface of particles with a Maxwellian velocity distribution characterized by a mean energy whose value lies between that of the incident particles and that corresponding to the actual surface temperature. Instead of measuring the actual distribution of reflected particle velocities, measurements of more readily attainable macroscopic properties have been relied upon. The so-called energy and momentum "accommodation coefficients" have been defined, providing gross representations of the nature of gas-surface interaction.

A natural extension of present knowledge of the problem would therefore be to measure the actual distribution of velocities.

Recent efforts at the University of Virginia have been concerned with such measurements. A high-intensity nozzle-type molecular beam together with a sensitive time-of-flight detection system developed by Hagen, et al.⁽⁴⁾ has been used to determine the velocity distribution of the particles after scattering from solid surfaces; preliminary results have been presented by Hagen⁽⁵⁾.

The time-of-flight method consists of measuring the times required for particles to travel a known distance. With the present method, the relative distribution of particle flight times may also be observed; the resulting time-of-flight distribution is straightforwardly related to the particle speed distribution. Such measurements have been made using argon and nitrogen as beam gases incident on polycrystalline nickel targets. The effects of target temperature, temperature history, and angle of incidence have been studied.

Results are presented in terms of both the angular and time-of-flight distributions of reflected particles along with certain parameters which characterize the time-of-flight distributions. An analysis is made of a method of fitting analytical expressions to the measured time-of-flight distributions, and a comparison of the resulting moments is made with those obtained by numerical integration. The overall results are then discussed in relation to certain simple theories.

SECTION II

EXPERIMENTAL APPARATUS

2.1 INTRODUCTION

The vacuum system and nozzle-beam source used for the present scattering experiments were developed by Hagen, et al.,⁽⁴⁾ and a complete description of the system along with beam characteristics and an analysis of the time-of-flight (TOF) method is given in that report. The following description is a summary of the important characteristics of the apparatus pertaining to the scattering experiments together with details of the target.

2.2 VACUUM SYSTEM

The vacuum system consists of a cylindrical tank divided into three chambers, each of which has separate pumping. The test chamber occupies a pie-shaped 243° sector. Gas from a high-pressure bottle source expands through a 0.06 mm diameter nozzle into the exhaust chamber. The core of the expanded jet is then skimmed off and collimated and enters the target chamber with an angular spread of about $\pm 2^\circ$ and a beam diameter of about 5 mm at the target. The relative location of the various components is shown in Figure 2.2.1. A test chamber pressure of about 10^{-8} torr

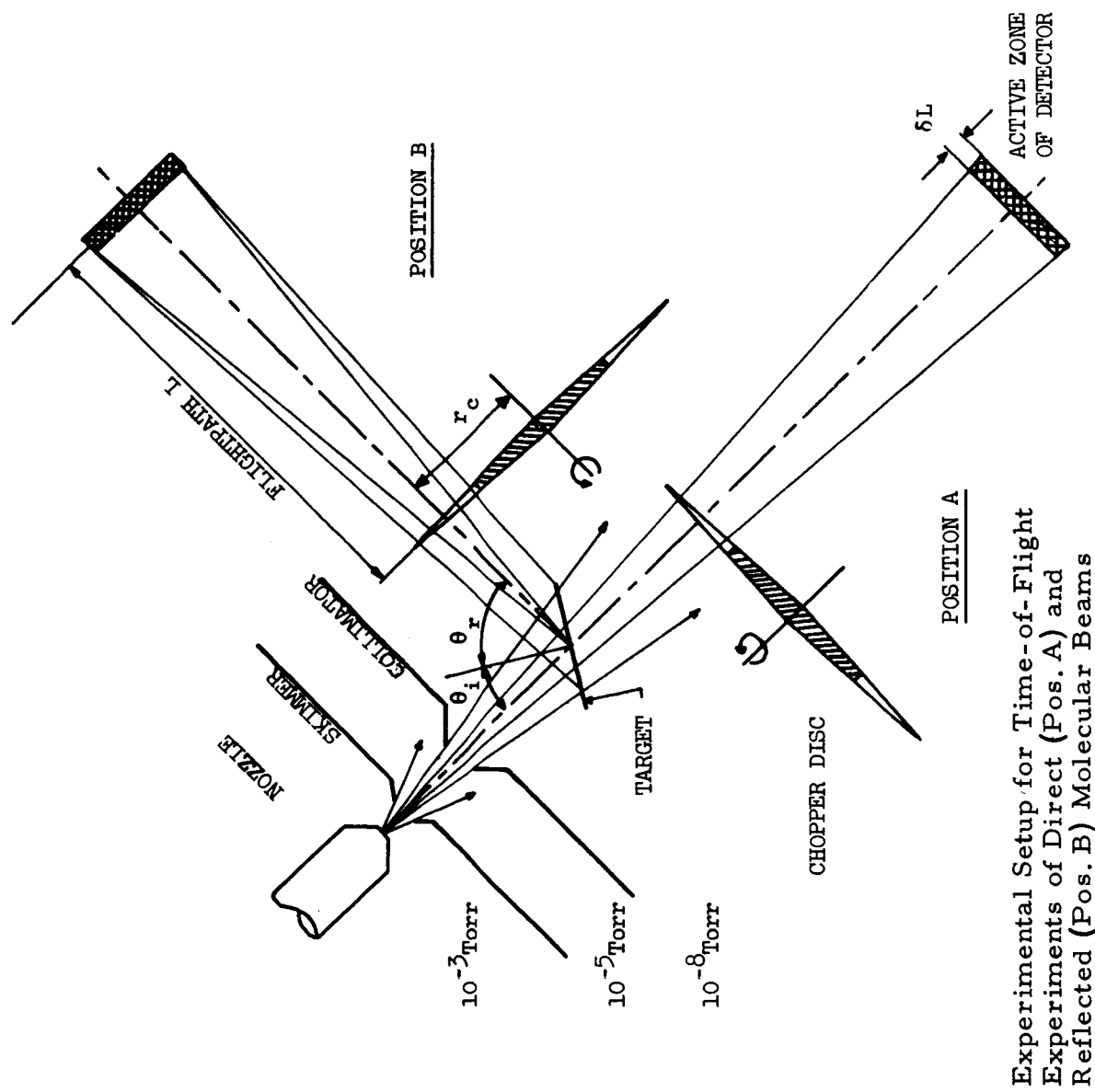


Figure 2.1.1.1

Experimental Setup for Time-of-Flight
Experiments of Direct (Pos. A) and
Reflected (Pos. B) Molecular Beams

is observed without the gas load of the beam; however, this pressure increases to about 10^{-7} torr with the beam in operation.

2.3 BEAM SOURCE

Room temperature sources of argon and nitrogen were used for the present experiments at typical source pressures of about 1420 and 2860 torr respectively. At these pressures, incident molecular beam speed ratios of 18.5 and 13.6 were measured for argon and nitrogen, respectively, with incident beam "currents" of about 1.6×10^{16} particles/sec. for both gases.

2.4 TARGET

Polycrystalline targets of unpolished nickel stock with a manufacturer's stated purity of 99.97% were used. Each target was mounted on a stainless steel block as shown in Figure 2.4.1 and chemically cleaned before installation in the vacuum chamber. A coiled tungsten filament, installed inside the heater block and connected to a 12 volt d. c. power supply, heated the target to temperatures as high as 1000°K. The filament was usually biased at a positive potential to suppress electron emission at high filament temperatures. A chromel-alumel thermocouple, connected at the top of the target surface, measured the surface temperature. The junction of this thermocouple was made small

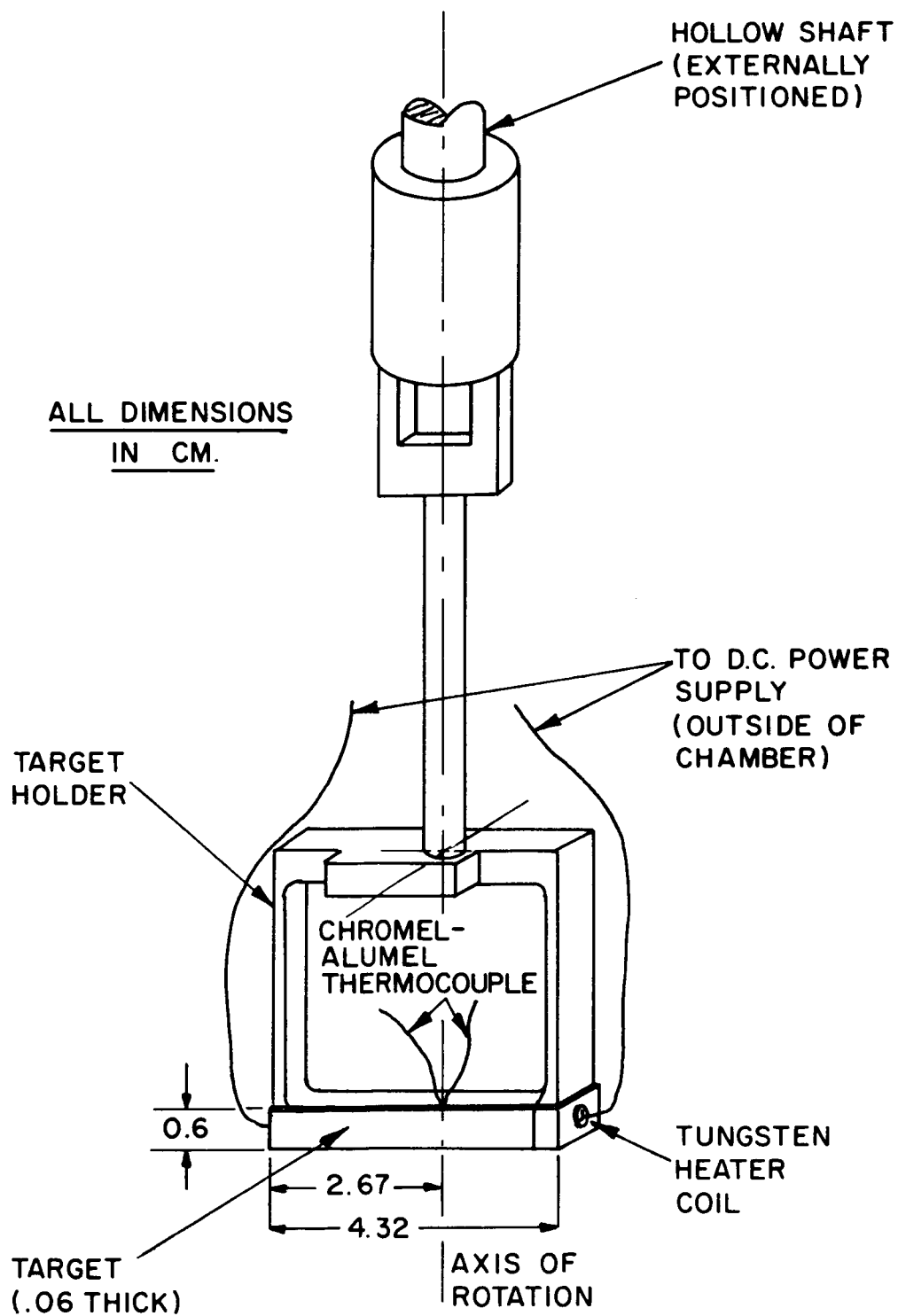


Figure 2.4.1 Target and Holder

compared to the target dimensions to prevent any appreciable scattering of beam particles and to prevent any appreciable heat conduction away from the target.

The vertical axis of the target holder was located in the center of the cylindrical vacuum tank. The target could be positioned externally in three-dimensions (for alignment) and could be rotated 360° about the vertical axis for varying the angle of incidence. The target axis was aligned, by optical methods, coincident with the centerline of the vacuum chamber. (The centerline of the incident molecular beam intersects the tank centerline in a right angle. The detector rotates in an arc centered at this intersection.) Then, the target elevation was adjusted such that the beam centerline intersected the target axis at the target midpoint. The position of the target midpoint with respect to the incident beam centerline was determined by observing the intensity of the direct beam downstream of the target as a function of target elevation (with $\theta_i = 0$). With this method of alignment, the position of the target midpoint was known to be within ± 0.5 mm of the center of rotation of the detector. The angular position of the target, indicated on a polar scale located outside the chamber, could be read to within $\pm 0.5^\circ$. Due to the geometry of the time-of-flight detection system, the limiting angle of incidence θ_i was determined by the condition that the detector should see the entire target area illuminated by the incident beam. For an

incident beam diameter of 5 mm at the target, the maximum angle of incidence was 74° . Therefore, true spatial distributions of reflected beam particles could not be measured for $\theta_i > 74^\circ$.

Three target specimens from the same stock were used (hereafter referred to as Nickel I, II, and III). Each was subjected to a different "heat treatment," the effects of which will be discussed in detail in Section 4.1. Nickel I and II were rectangular flats, while Nickel III was bent into a U-shaped channel with the sides of the U extending over the top and bottom of the heater block. The latter design was chosen in an attempt to produce a more uniform temperature distribution across the surface at high target temperatures. To observe this distribution for a heated target, reflected beam measurements were made at an indicated surface temperature of about 900°K with the target normal to the beam centerline ($\theta_i = 0^\circ$) while moving the target across the incident beam. Relative changes in reflected beam characteristics gave an indication of the variations in local surface temperature. Measurements indicated that this variation was much less for the Nickel III configuration than for the Nickel I-II configuration. Therefore, measured target temperatures likely do not reflect the mean surface temperature as closely for Nickel I and II.

2.5 TOF METHOD

After scattering from the target, the beam particles pass through a slotted rotating disk (or chopper) which produces short pulses of particles. The particle pulses then spread, according to the relative distribution of particle speeds in each pulse, in their transit from the chopper to an ionization detector (sensitive to instantaneous particle density) which monitors their time of arrival.

The chopper and detector are mounted on a table which can be rotated over an angular range of 200° about the target midpoint. All present measurements are limited to the plane formed by the incident beam axis and the target normal.

Chopper - The chopper is designed consistent with the resolution requirements as set forth in reference (4). The chopper wheel has a mean radius of 7.6 cm and has four equally spaced slits with a slitwidth of 0.508 cm. Typical chopper peripheral speeds were about 0.6×10^4 cm/sec for room temperature target experiments and about 1.0×10^4 cm/sec for hot targets. A light-photocell pickup is located on the side of the chopper opposite the beam to mark the zero in the flight time. A distance of 5.1 cm from target midpoint to chopper and a flightpath L from chopper to detector of 25.4 cm were used for all scattering experiments.

Detector - The detector was of the through-flow ionization type, as documented by Hagena, et al. ⁽⁴⁾ After passing through the chopper, beam particles enter the active zone of the detector where a small fraction of the particles are ionized by a bombarding electron beam entering normal to the reflected beam. The collected ions form a current proportional to the average instantaneous particle density over the active zone of the detector. This current is passed across a load resistor R_L ; the voltage drop across this resistor is amplified, passed through a signal-averaging device to reduce signal noise, and recorded on an x-y plotter. The final detector signal at a given time t is then

$$S_d(t) = i^+(t) \times R_L \times \text{Amplifier-Gain.} \quad (2.1)$$

The ion current $i^+(t)$ is related to the instantaneous average density $n(t)$ over the active zone of the detector as follows:

$$i^+(t) = i^- \times \sigma_{\text{eff}} \times l_{\text{eff}} \times n(t) \quad (2.2)$$

where i^- = ionizing electron beam current, σ_{eff} = the effective ionization cross-section between electrons and beam particles and l_{eff} = the electron path length in the active zone of the detector. Therefore, the recorded detector signal $S_d(t)$ may be converted to units of detector particle density if all of the quantities on the right side of Equations (2.1) and (2.2) are known.

The unknowns in the latter equation are determined by calibration with a direct molecular beam of known density.

SECTION III

DATA REDUCTION

3.1 PARAMETERS OF THE TOF CURVE

In order to simplify the analysis of the TOF distributions, it is convenient to describe them by certain characteristic times. Figure 3.1.1 is a reproduction of some actual recordings of TOF distributions at various angles of reflection θ_r for nitrogen scattered from a room temperature target. The signal analyzer divides the measured signal into 100 equal time intervals; each step in the curves corresponds to one of these intervals. The signal from the photocell at the beginning of each curve marks approximately the zero in the time-of-flight. Added to the figure are the relation of signal height to particle density, the TOF scale, and three characteristic times.

TOF at Maximum Signal - The TOF at maximum signal t_m is used to give an indication of the average particle speed. For an ideal oven-beam or high speed ratio nozzle-beam TOF distribution, t_m is directly related to the mean speed. For the present TOF distributions of scattered beams the exact relation between t_m and mean speed must be obtained by numerical integration.

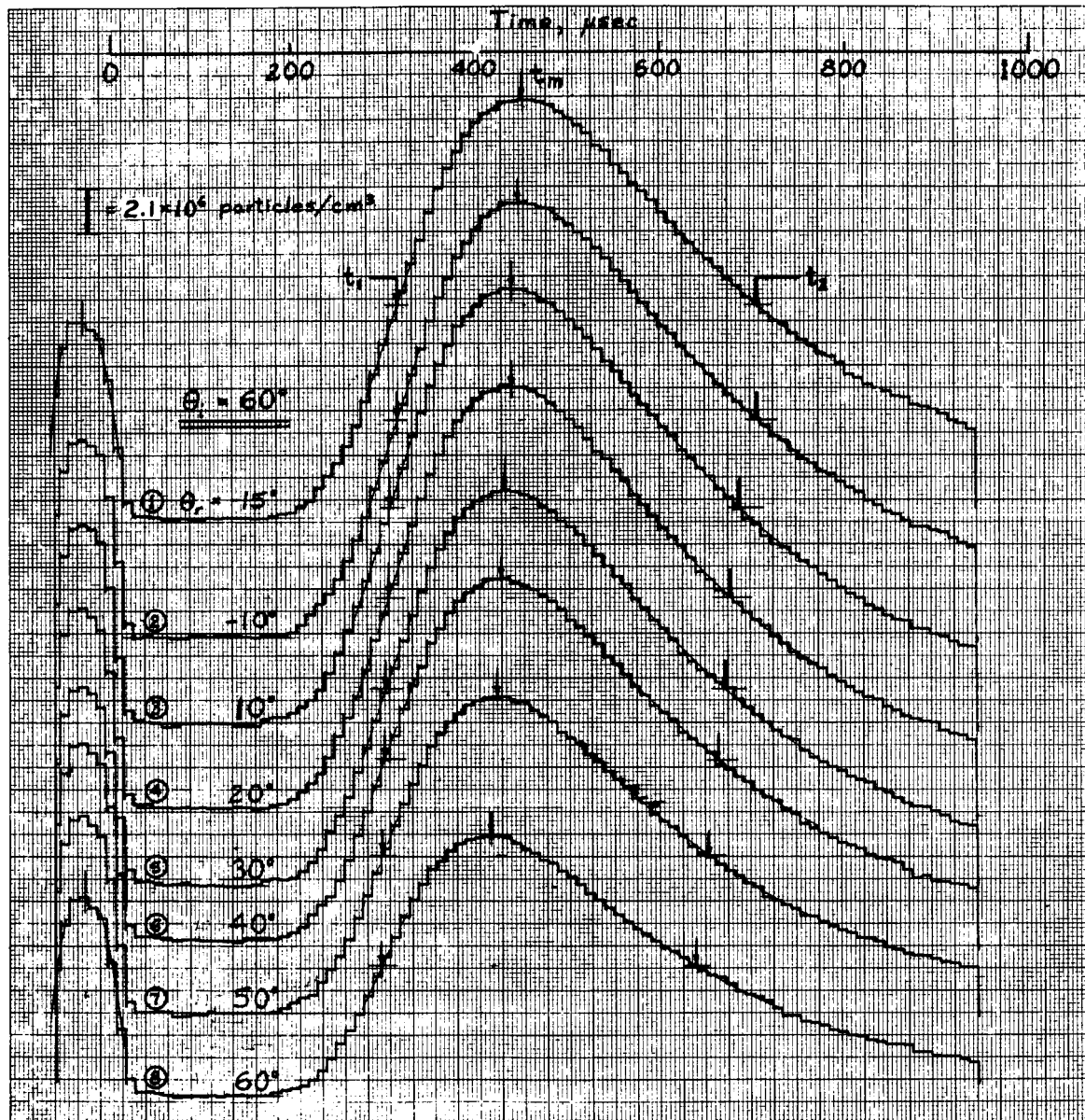


Figure 3.1.1 Sample Recording of TOF Distributions

TOF at Half-Maximum Signal - The width of the distribution $\Delta t = t_2 - t_1$ at half-maximum signal is indicative of the thermal velocity spread, where t_1 and t_2 are the TOF's at half-maximum signal ($t_1 < t_2$). The ratio $t_m/\Delta t$ is indicative of the speed ratio S . For an ideal oven-beam distribution, one can show that $t_m/\Delta t$ has the value 1.08 independent of temperature, while for a high speed ratio nozzle-beam ($S \gg 1$), its value is given approximately⁽⁴⁾ by

$$t_m/\Delta t \approx S/1.67. \quad (3.1)$$

Therefore, this ratio is useful for comparing the experimental TOF distributions with that for an oven-beam or the incident nozzle-beam.

The quantity t_2/t_1 is used as a parameter for fitting given analytic expressions to the experimental distributions and will be discussed in Section 3.2, and the Appendix.

Determination of Flux - An approximate parameter of the experimental TOF distribution is used in lieu of the true reflected flux. It is given by

$$I \approx \frac{S_d(t_m) \cdot \Delta t}{t_m \tau} \quad (3.2)$$

where $S_d(t_m)$ is the maximum signal height and τ is the half-width of the shutter function, i. e., the initial pulse width at half-maximum, as defined by Hagena, et al.⁽⁴⁾ The quantity

$S_d(t_m) \cdot \Delta t/T$ is proportional to the scattered beam density n_o if the beam were not chopped, and $1/t_m$ is approximately proportional to the average speed. If the TOF distributions are functionally similar at all angles of reflection (i. e., may be reasonably expressed in some common analytic form), the given expression is a valid first approximation for obtaining the scattered flux distribution. Since an exact expression for I would involve numerical integration of the experimental distributions, which for the present results would not be a worthwhile task, Equation (3. 2) is used to give a qualitative picture of the scattering process. The quantity I in the data is then that given by (3. 2).

3.2 MOMENTS OF THE TOF CURVE

The measured TOF distributions provide detailed information relatable to the scattering process. It is helpful to know certain average properties (or moments) of the reflected distributions, i. e., mean translational momentum and energy of reflected particles. These moments may be calculated either by numerical integration of the measured distribution or by direct integration of some analytical expression which accurately represents the experimental distribution.

Numerical Integration - It is straightforward to show that the average translational momentum of particles leaving the surface

at a given angle θ_r is given by

$$m\bar{v} = \frac{mL \int_0^{\infty} \frac{S_d(t)}{t^2} dt}{\int_0^{\infty} \frac{S_d(t)}{t} dt} \quad (3.3)$$

where $S_d(t)$ is the measured TOF distribution (or detector signal) and the integral represents numerical integration over time space. Similarly, the average translational energy is

$$\frac{1}{2}m\bar{v}^2 = \frac{\frac{1}{2}mL^2 \int_0^{\infty} \frac{S_d(t)}{t^3} dt}{\int_0^{\infty} \frac{S_d(t)}{t} dt} \quad (3.4)$$

Equations (3.3) and (3.4) may be applied directly to any experimental TOF curves if the resolution $R = \Delta t/T$ is sufficiently great so that the TOF curve-shapes are independent of R , i.e., are directly related to the speed distribution in the unchopped beam. If the resolution is not sufficient, the moments must be determined by the inversion of a convolution integral involving the shutter-function. This integral has been evaluated by Hagena, et al. ⁽⁴⁾, for a triangular shutter function using ideal oven-beam and nozzle-beam distributions, giving the measured Δt in terms of the ideal half-width Δt_0 as a function of R . Using corrections derived from this analysis, the effects of resolution on low-order moments have been estimated for

the present experiments using the curve-fitting method outlined below. It shows that in the resolution range used the moments should not be in error by more than 3%. (See Appendix.)

Moments from Fitted Curve - While the numerical integrations involved in Equations (3.3) and (3.4) are simple, their use would be overly time consuming for the present experiments. Another method for obtaining the desired moments has been applied here. It fits a fixed functional expression with four free parameters to the measured TOF distribution. The moments are then functions of these parameters. The functional form used is

$$S_d(t) \propto \frac{n_o}{t^n} \exp[-\beta^2 L^2 (\frac{1}{t} - \frac{1}{t_o})^2] \quad (3.5)$$

where the four free parameters are n_o , β and t_o (which for the functional form are indicative of beam density, beam thermal spread, and mean speed, respectively) and a free fitting exponent n . The corresponding relative distribution of reflected flux dI/dv is

$$dI/dv \propto n_o v^{n-1} \exp[-\beta^2 (v - v_o)^2] \quad (3.6)$$

where $v_o = L/t_o$. For qualitative discussion, $S_d(t)$ is normalized so that n_o is no longer important. The two parameters β and S ($\equiv \beta L/t_o$) can be adjusted such that $S_d(t)$ fits the measured

distribution at the two points t_1 and t_2 . In the Appendix procedures required for this type of curve fitting are described in detail, and a comparison is made between moments obtained by this method and those obtained by numerical integration. The results of this analysis indicate that Equation (3.5) provides a reasonably accurate fit for the measured TOF distributions and yields moments which agree within 5% of those numerically computed for the curves which were analyzed.

SECTION IV

EXPERIMENTAL RESULTS

4.1 "DIRTY" ROOM TEMPERATURE TARGET

Flux Distribution - For a "dirty" room temperature target with both argon and nitrogen incident beams, the distribution of scattered flux is almost completely random as shown in Figure 4.1.1. By "dirty" it is implied that no attempt has been made to outgas the surface and no type of heat treatment has been given that would affect the crystal structure. Therefore, the target was covered by a layer of adsorbed gases and had the crystal structure of the material as rolled. The solid line shown in Figure 4.1.1 is for diffuse reflection in which the direction of scattered particles would be completely random resulting in a flux distribution which is proportional to $\cos \theta_r$ (usually referred to as cosine-law scattering). Both argon and nitrogen show a slight lobular (or preferential) type of scattering compared with purely diffuse reflection; however, this slight disagreement is within the limits of the approximate method used to determine the flux I from the experimental TOF distribution. The earlier measurements of Hurlbut⁽⁶⁾ show a similar type of spatial distribution for various gases and targets.

All flux measurements for Figure 4.1.1 and subsequent data have been normalized by I_0 which is the measured flux

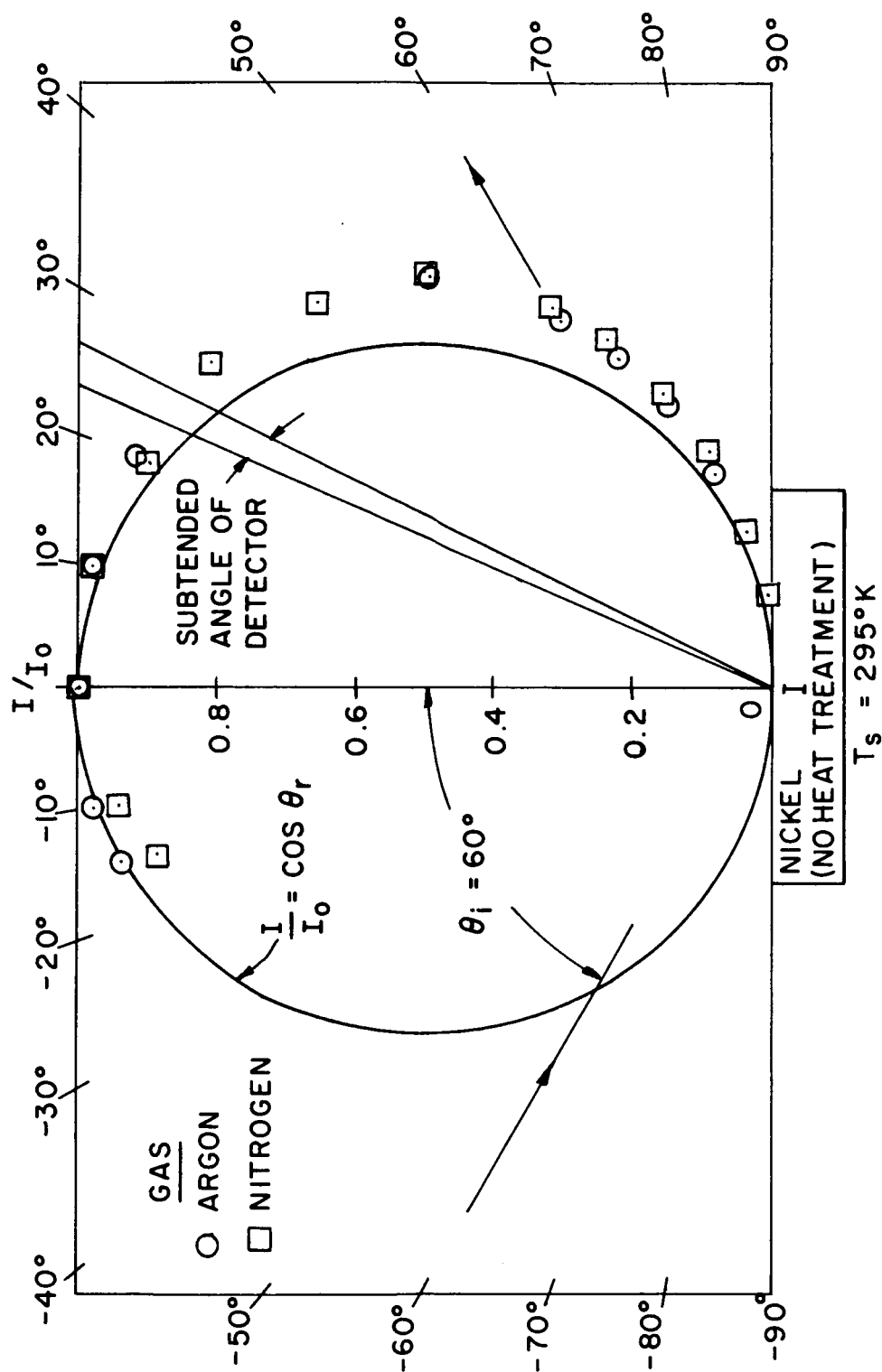


Figure 4.1.1 Flux Distributions for Argon and Nitrogen Beams Scattered from a Room Temperature Target

at $\theta_r = 0$ for the condition of a "dirty" room temperature target. (Measured values of I_0 for argon and nitrogen differ by about 20%.) The ratio I/I_0 may then be used as a comparison of other data with this random type of scattering and gives the relative "lobularity" of other reflected flux distributions. "Lobularity" is used loosely here and afterwards to characterize the maximum degree of variation of I from that for cosine-law scattering. To check the absolute magnitude of the value for I_0 , the total incident flux was calculated using I_0 and assuming completely diffuse scattering. This calculated value is 10% less than the total incident flux measured by Hagena, et al. ⁽⁴⁾ for argon and about 10% greater for nitrogen. These disagreements reflect the errors in assuming complete diffuse scattering and in the approximate methods of obtaining the flux from the measured TOF distribution, as well as a known uncertainty in the values of the incident flux for the present experiments.

TOF Distribution - Measured TOF distributions (for the same reflected nitrogen data of Figure 4.1.1) are shown for two angles of reflection in Figure 4.1.2 in comparison with a Maxwellian-type distribution corresponding to the effusion from the target surface at the measured target temperature. The Maxwellian TOF distribution would be expected for complete accommodation of the incident gas to the energy of the surface. It has the functional form

$$S_d(t) \propto \frac{1}{t^4} \exp(-\beta_s^2 L^2/t^2) \quad (4.1)$$

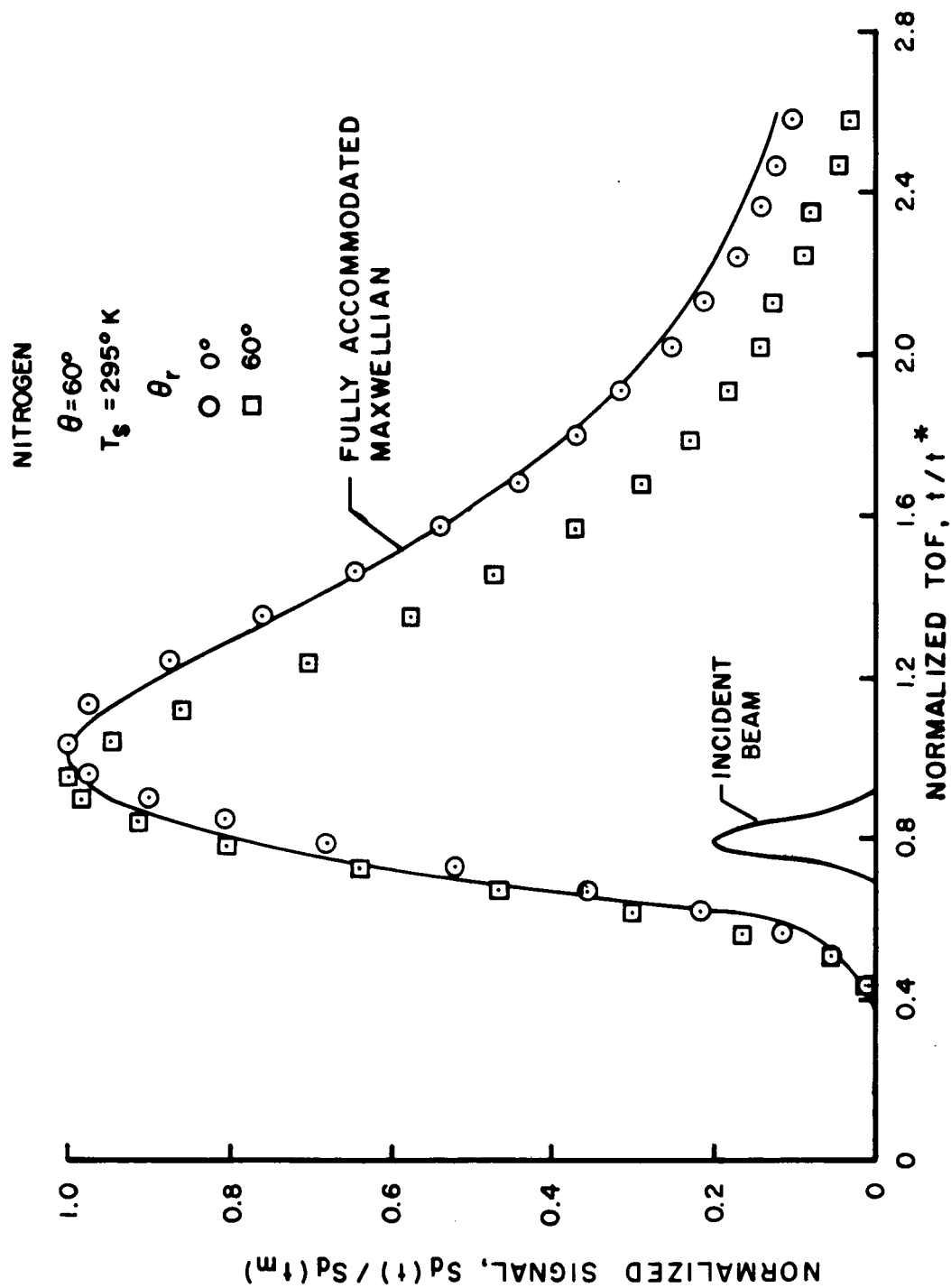


Figure 4.1.2 Comparison of Measured Reflected Beam TOF Signals with that Predicted for Maxwellian Effusion with Full Thermal Accommodation

where $\beta_s = \sqrt{m_g/2kT_s}$. The measured TOF distribution for particles scattered normal to the target ($\theta_r = 0^\circ$) agrees relatively well with the predicted curve, although there is a deficiency of measured particles on the low-time (high-speed) side of the distribution. Also, the measured t_m is slightly larger. At $\theta_r = 60^\circ$, the measured TOF distribution is considerably more narrow than the fully accommodated Maxwellian and the measured t_m reflects a higher mean speed. This indicates that the reflected beam tends to appear more like the incident beam whose half-width and t_m are shown in this same figure. Similar results were observed for argon. Therefore, the scattered particles exhibit a varying degree of accommodation to the surface energy as a function of angle of reflection.

The measured signals have been normalized to unity at their maximum and the time-of-flight normalized by t^* , the time at which the maximum occurs in the fully accommodated Maxwellian distribution. The ratio of t_m to t^* for any measured distribution, therefore, gives an indication of the degree to which the scattered particles have been accommodated to the surface temperature.

4.2 EFFECT OF SURFACE TEMPERATURE AND TEMPERATURE HISTORY

For low incident beam and target temperatures where the energy difference is very small, it is seen here that

the spatial distribution of scattered particles is reasonably that for diffuse reflection. However, marked deviations were observed by Smith and Fite⁽⁷⁾ and Hinchey and Foley⁽⁸⁾ with various gases and targets for certain beam and target temperatures. These deviations were such that the scattering patterns were highly preferential even for polycrystalline targets. With the present apparatus, it was desired to reproduce at least the qualitative nature of these scattering experiments so that the addition of speed distribution measurements would provide a more complete picture of the scattering processes.

Effect of Temperature History at Fixed θ_r - Starting
 with a room temperature target which had nearly a cosine distribution of flux, the target temperature was increased continuously to 1000°K and then allowed to cool to about 900°K where it was kept constant for several hours. With a nitrogen beam at $\theta_i = 60^\circ$, the signal height $S_d(t_m)$ was monitored with the detector at $\theta_r = 60^\circ$. At this angle of reflection, an increase in $S_d(t_m)$ corresponds to an increase in the lobularity of the scattering pattern. The results of this heat treatment are shown in Figure 4.2.1 as a function of heating time. Since about three minutes were needed to average and record a TOF signal, measurements made during unsteady conditions are in error to that extent.

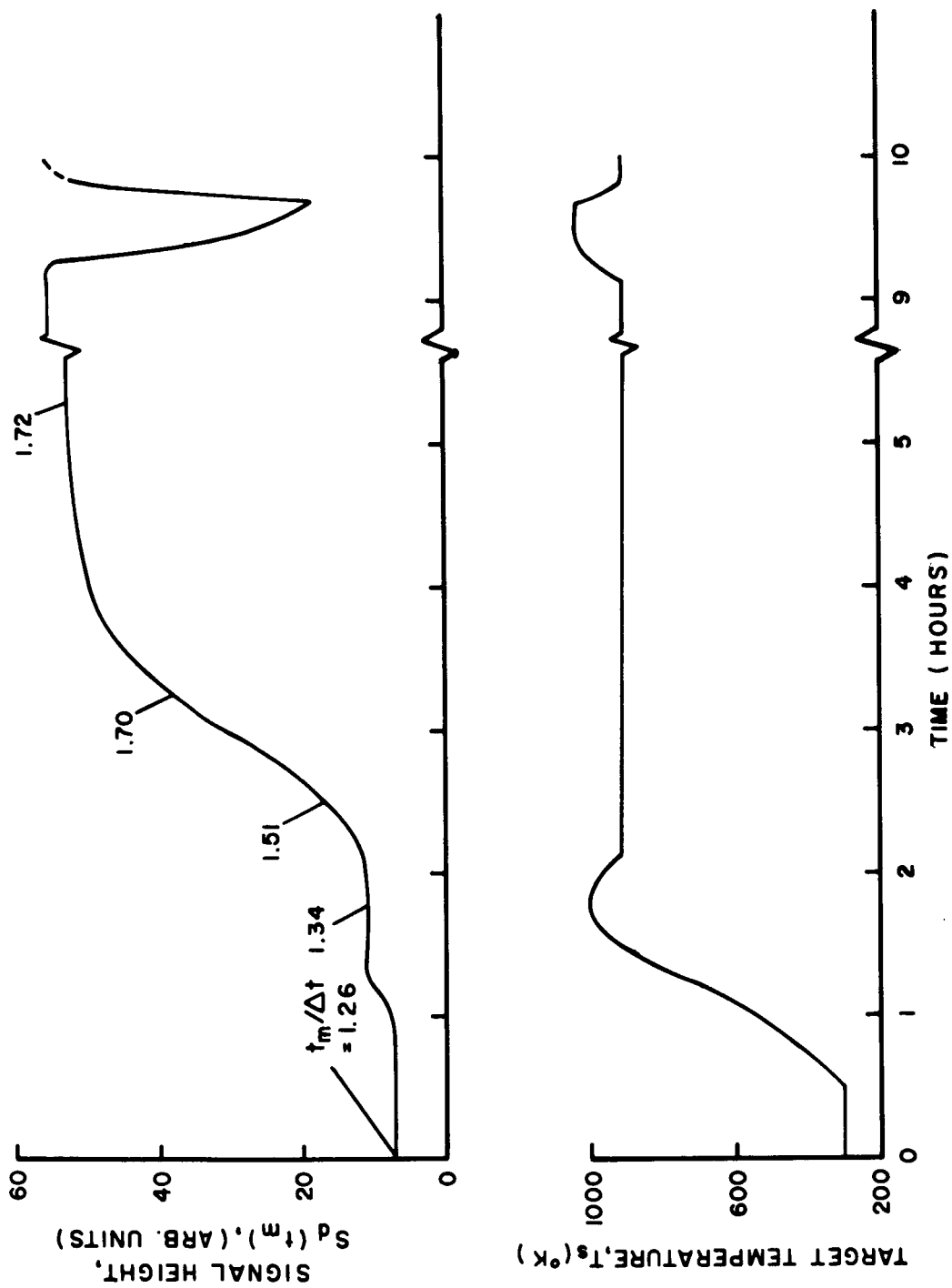


Figure 4.2.1 Time History for Scattered Nitrogen Beam
Signal Height with Target Temperature
Variation, $\theta_i = \theta_r = 60^\circ$, Nitrogen Beam Gas

It is seen that the increase to 1000°K does not greatly change $S_d(t_m)$ or $t_m/\Delta t$, while heating at 900°K for a period of several hours produces a highly lobular type of pattern with an accompanying increase in $t_m/\Delta t$. After the measured $S_d(t_m)$ had reached a final steady-state value, the temperature was again increased to about 1000°K. The result was that the lobularity tended to be destroyed as shown by the sharp decrease in $S_d(t_m)$. However, cooling back to 900°K caused an almost immediate return to the lobular behavior.

The results in Figure 4.2.1 are for Nickel II. Similar results were observed for Nickel III, although the magnitude of the lobularity was slightly different.

As a result of these experiments, it was found that two distinct types of target conditions occurred. For convenience in discussing the following data, "heat treatment" is defined as heating in a vacuum for several hours at $900 \pm 50^\circ\text{K}$. Conditions before prolonged heating at 900°K will be referred to as "dirty" target conditions. "Clean" target conditions existed only after heating at 900°K for several hours. Descriptions of target conditions as "clean" and "dirty" are used for qualitative discussion only and do not necessarily describe true surface conditions which present experiments do not yield. Heating at 1000°K destroys the results of previous "heat treatment" and produces results similar to those before heat treatment.

Effect of Heat Treatment on Reflected Spectrum

(a) "Dirty" Target - A comparison of the scattered nitrogen beam parameters as a function of θ_r is given in Figure 4.2.2 for various target temperatures. Figure 4.2.2(a) shows the results for "dirty" target conditions and indicates a relatively diffuse spatial distribution for all three target temperatures, being only slightly lobular at the higher temperatures. A list of the important steps of the "heat treatment" for Nickel II and the resulting flux distribution is given below in chronological order:

<u>"Heat Treatment" Nickel II</u>	<u>Flux Distribution</u>
(1) 295°K	Nearly cosine
(2) 1025°K for several hours	Slightly lobular
(3) Cooled quickly to 771°K	Slightly lobular
(4) 295°K	Nearly cosine
(5) 903°K for several hours	Highly lobular
(6) Cooled to 295°K	Slightly lobular
(7) 903°K for several hours	Highly lobular
(8) Cooled to 545°K	Highly lobular
(9) 1025°K for few minutes	Slightly lobular

The data for $T_s = 295^\circ$ and 771°K in Figure 4.2.2(a) were obtained in steps (3) and (4) and therefore indicate that no permanent change occurred in the surface structure even by

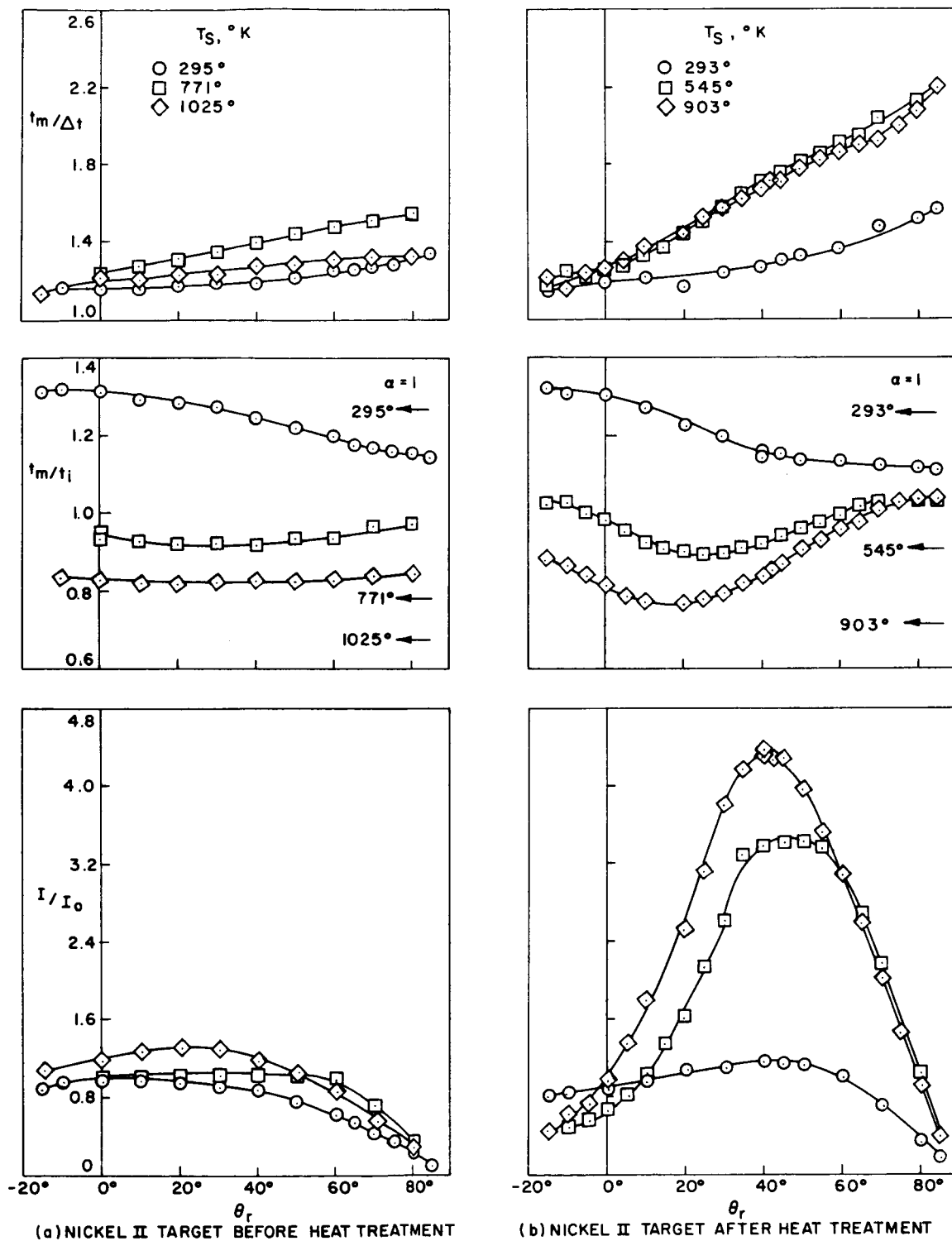


Figure 4.2.2 Variation of I/I_0 , t_m/t_i , and $t_m/\Delta t$ with Scattering Angle: Nitrogen Beam, $\theta_i = 60^\circ$

prolonged heating at 1025°K. Of further note, the results shown at $T_s = 1025^\circ\text{K}$ were actually independent of any previous heat treatment at lower temperatures. This unique behavior due to heating at 1025°K was quite repeatable; however, the exact cause is still uncertain.

The variations of t_m/t_i (where t_i is the TOF at maximum signal for the incident beam) and $t_m/\Delta t$ (which is an indication of the speed ratio) show that accommodation to the surface temperature varies slightly as a function of θ_r . For complete accommodation, while $t_m/\Delta t$ has the constant value of about 1.08, the values of t_m/t_i are indicated by arrows for the different temperatures. At the higher target temperatures, t_m for the reflected beam is always less than that for the incident beam, but greater than that corresponding to complete accommodation. For a room temperature target, t_m for the reflected beam is always greater than that for the incident beam; however, the degree of accommodation depends more strongly on the angle of reflection. The values of $t_m/\Delta t$ are always greater than that for complete accommodation for all three temperatures but always less than for the incident beam ($t_m/\Delta t \approx 8$ for the incident N_2 beam).

(b) "Clean" Target - As was indicated in Figure 4.2.1, prolonged heating at 900°K caused a definite change in the scattering process. The result is that the spatial distribution tends to be more specularly directed. Although true specular reflection, i. e., no change in velocity and $\theta_r = \theta_i$, does not occur, the flux distributions become highly lobular at elevated

target temperatures as seen in Figure 4.2.2(b). The distribution at room temperature is also more lobular than for "dirty" target conditions, indicating a permanent change in surface conditions. This lobular type of scattering for "clean" targets was always reproducible by prolonged "heat treatment" at about 900°K as seen in the target history on page 28. Lobe maxima do not occur precisely at the specular angle, but are shifted away from the specular angle toward the surface normal. This shift is also observed by Hinchey and Foley⁽⁸⁾.

There are also differences in the TOF distributions for "clean" and "dirty" conditions. Values for t_m/t_i show larger variations with θ_r for a target after heat treatment than before heat treatment and have definite minima (corresponding to maximum thermal accommodation). However, the angular locations of these minima do not show any definite correlation with the maxima in the flux distributions. Average velocity measurements by Hinchey and Malloy⁽⁹⁾ and TOF measurements by Moran, et al.⁽¹⁰⁾, confirm this angular dependence of accommodation with the latter showing variations of t_m with θ_r similar to the present results. At large angles of reflection, $t_m/t_i > 1$ suggests negative thermal accommodation. For a true representation of momentum and energy accommodation, taking into account the thermal spread in the distributions, the accommodation would likely still be positive. The ratio $t_m/\Delta t$

is much larger, for $\theta_r > 0^\circ$, after heat treatment and increases almost linearly with θ_r for $T_s = 545^\circ$ and 903°K . However, a maximum value of 2.2 for $t_m/\Delta t$ indicates clearly that the effect of the scattering process is still to greatly increase the thermal velocity spread over that of the incident molecular beam.

4.3 EFFECTS OF ANGLE OF INCIDENCE AND BEAM GAS MOLECULAR WEIGHT

Angle of Incidence - Preceding results have corresponded to a single angle of incidence. The effects of varying angle of incidence were measured using Nickel II at a temperature of 903°K and are presented in Figure 4.3.1(a). This temperature was selected because this data shows the most pronounced variations. Lobular flux distributions were observed for all three incident angles. The angular position of the lobe maxima increases with increasing angle of incidence as does the deviation of the maxima from the specular angle. The width of these lobes at half maximum does not vary greatly with angle of incidence.

The TOF distributions show similar variations with θ_r for all three incident angles. Maximum accommodation occurs for $\theta_i = 70^\circ$ based on t_m/t_i and for $\theta_i = 40^\circ$ based on values of $t_m/\Delta t$. This further illustrates that a clear picture of momentum and energy accommodation must be obtained from the moments

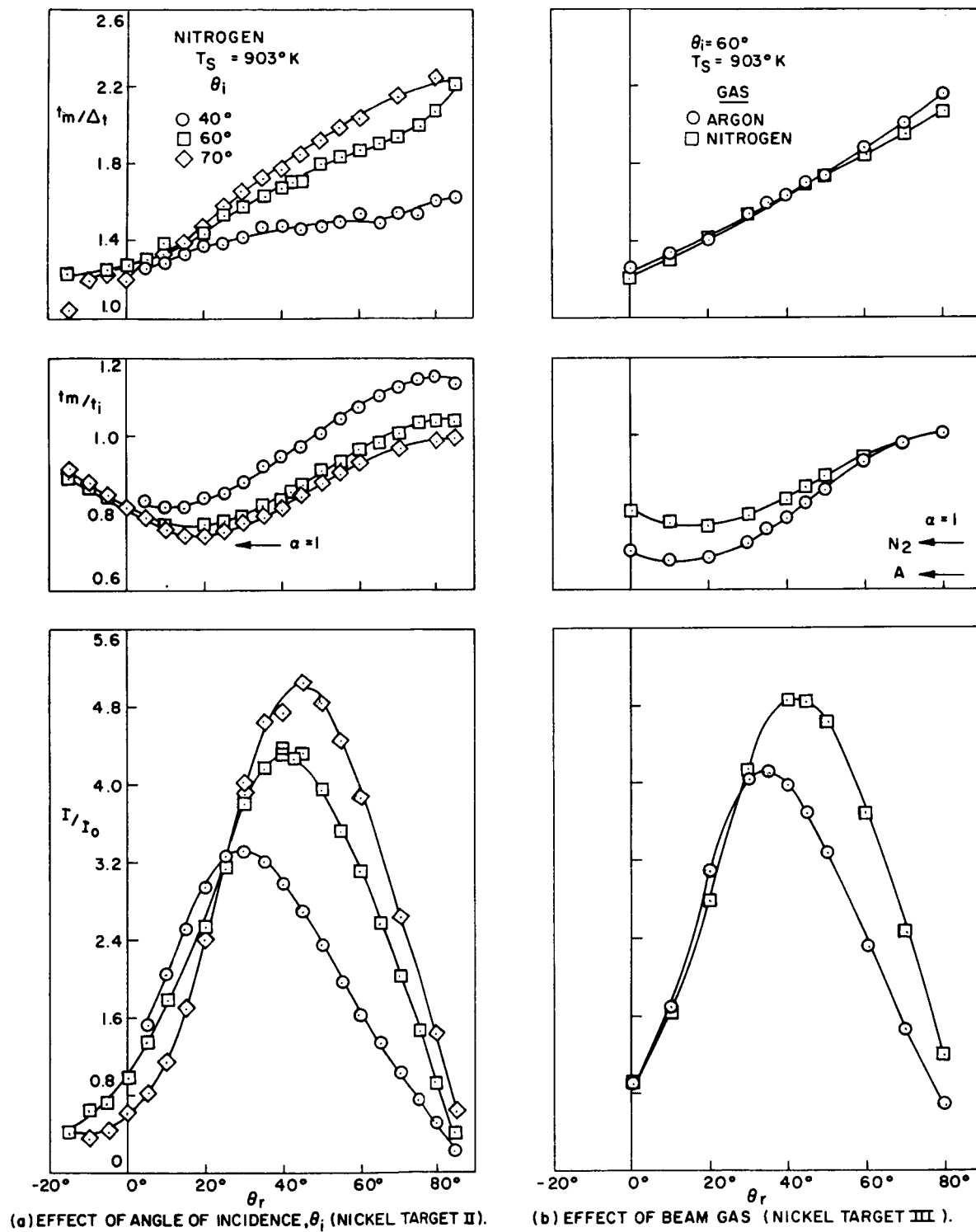


Figure 4.3.1

Effect of Angle of Incidence and Beam Gas
on I/I_0 , t_m/t_i , and $t_m/\Delta t$

of the measured distributions and not from these simple parameters.

Beam Gas Molecular Weight - Reflected beam characteristics are presented in Figure 4.3.1(b) for incident molecular beams of argon and nitrogen. It is seen that the general features of the scattering are not too different for monatomic argon and diatomic nitrogen. Both gases result in a lobular distribution of scattered flux with the displacement of the lobe maximum from the specular angle being greater for argon. The difference in maximum lobe heights may be a reflection of the slightly higher incident flux for nitrogen which resulted from using slightly different nozzle-skimmer separation from that used for previous data.

The TOF distributions show similar variations of t_m/t_i for the two gases, with both reaching $t_m/t_i = 1.0$ at $\theta_r = 80^\circ$. Variations in $t_m/\Delta t$ are almost identical for the two gases, with argon having only slightly higher values at large θ_r .

4.4 MODIFYING INFLUENCES ON THE DATA

Effect of Resolution - Chopper speeds were kept constant for a given set of measurements at a given target temperature. As a result, the resolution R varied due to changes in Δt for the

measured TOF distributions. Typical ranges for R were between 4 and 5. For $R = 5$ Hagena, et al. ⁽⁴⁾ show that measured values of Δt are 2% higher than for $R \rightarrow \infty$. All data presented so far have not been corrected for non-infinite resolution. The effect of resolution on the moments \bar{v} and \bar{v}^2 of the TOF distributions is discussed in the Appendix.

Changes in Incident Beam Flux - Experiments were conducted in which the incident beam flux was reduced by a factor of about 2 by increasing nozzle-skimmer separation in order to determine the effects of incident beam flux on the build-up of adsorbed layers of beam particles. Measurements at target temperatures of 295°K and 732°K show no appreciable effect on the observed TOF distributions due to reducing incident flux, with $t_m/\Delta t$ changing by less than 1% at the representative values of θ_r chosen for observation. Scattered flux patterns were also reproducible to within a few percent of the peak flux.

Changes in Background Pressure - For a typical test chamber pressure of about 10^{-7} torr, it is desirable that the magnitude of the flux of background particles incident on the target not affect the TOF measurements. With a nitrogen beam at $\theta_i = 60^\circ$ incident on a target at 900°K, the test chamber pressure was increased to 4×10^{-6} torr by bleeding air into the system. Measurements were made at $\theta_r = 0^\circ$ and 40° so that an indication of the effect on lobularity of the reflected

distribution could be obtained. This pressure increase caused a significant decrease in the lobularity of the scattering pattern, although the TOF distributions showed changes of only about 1% in $t_m/\Delta t$. Decreasing the pressure resulted in restoration of the low pressure scattering pattern as the pressure dropped below 10^{-6} torr. Also observed at a pressure 4×10^{-6} torr was an increase in the signal due to background particles with no incident beam. Increased background density will (a) increase the rate of background particles reflecting off the target into the detector and (b) increase the rate of background particles coming (not from the target) through the chopper and being detected (appearing to come from the target). The measured background signal at this higher pressure with beam off was about 5% of the total signal with the beam on at $\theta_r = 40^\circ$; however, at a normal chamber pressure of about 10^{-7} torr, no background signal was detected with the beam off. Therefore, in the range of normal operation, the measured signals were not significantly affected by background particles.

4.5 REPEATABILITY

The repeatability of the data was limited primarily by the reproducibility of surface conditions. As pointed out, the results were not affected appreciably by variations in incident

beam flux or background particle flux. Measurements with the so-called "dirty" targets usually gave better repeatability than the "clean" targets. Agreement for "dirty" targets was about 3% for I and $t_m/\Delta t$ measured on various dates for targets which were, for all experimentally controllable conditions, the same. Results with a "clean" target were influenced somewhat by the exact temperature history of the target. Therefore, quantitative measurements for these did not repeat as well as for "dirty" targets. Above this, the variations of all of the observed parameters were qualitatively the same for all repeated experiments. An example of this reproducibility may be seen by comparing the nitrogen data at $\theta_i = 60^\circ$ for Nickel II (Figure 4.3.1(a)) with that for Nickel III (Figure 4.3.1(b)).

In general, the experimental TOF measurements are more repeatable since they are not affected as strongly by heat treatment as the flux distributions. TOF parameters t_m and Δt were repeatable to within about $\pm 2\%$ for all comparable experimental conditions.

SECTION V

COMPARISON TO VARIOUS MODELS

5.1 DIFFUSE REFLECTION MODEL

One of the earliest models for gas-surface interactions is the diffuse reflection model⁽¹¹⁾. Two basic assumptions made with regard to the interaction are as follow : (1) The direction of the velocities of the gas molecules, after impact, will have a completely random distribution. This results in the so-called "cosine law" in which the flux re-emitted into any given unit solid angle is given by

$$I = I_o \cos \theta_r \quad (5.1)$$

where I_o = the flux emitted normal to the surface. (2) The re-emitted gas molecules will have a fully-accommodated Maxwellian speed distribution as if the molecules effused from an oven source located on the surface, such source in thermal equilibrium at the surface temperature.

Experimental measurements by Hurlbut⁽⁶⁾ support the first of these two assumptions, at least for cases in which the energy difference between the incident gas and the surface is small. Results from the present investigation also exhibit

reasonable agreement with the cosine law for a room-temperature incident beam and a room-temperature "dirty" target.

It has been found that the second of these assumptions is not necessarily valid even for small temperature differences.

The energy of the re-emitted gas does not always correspond to full accommodation. For this reason, a thermal accommodation coefficient was introduced⁽¹²⁾ and defined as follows:

$$\alpha = \frac{T_r - T_i}{T_s - T_i} \quad (5.2)$$

where the subscripts i, r, and s refer to the incident gas, reflected gas, and surface respectively. Similar expressions may be defined for accommodation of normal and tangential momentum. However, the relation (5.2) may be used only when the mean energies can be expressed in the form $2kT/m_g$. It is therefore applicable only when the velocity distributions of the incident and reflected particles can be represented by a Maxwellian function. Present results indicate this is not true, even in cases where the flux distribution may obey the cosine law (see Figure 4.1.2). A more general definition of accommodation must be used such as

$$\alpha_s(E_i, \vec{i}) = \frac{E_i - E_r}{E_i - 2kT_s/m_g} \quad (5.3)$$

where α_s is the accommodation coefficient for particles of energy E_i approaching the surface along vector \vec{i} and \bar{E}_r is the average energy of these particles upon reflection.

5.2 SPECULAR REFLECTION

Another simple type of interaction is that of specular reflection in which the particles interact elastically with the (assumed plane) surface with no change in momentum or energy. The angle of reflection therefore equals the angle of incidence, and the speed distribution of reflected particles is the same as that in the incident beam. Although true specular reflection was not observed in the present experiments, strong preferential scattering in the form of narrow lobes did occur for hot surfaces which had received a specific type of heat treatment (see Figures 4.2.2(b) and 4.3.1). However, the angular positions of the lobe maxima did not coincide with the specular angle but were displaced toward the surface normal; the positions of these maxima were also related to the target temperature, angle of incidence, and beam gas molecular weight. Measured TOF distributions show that the thermal spread in the scattered beam is always much greater than that of the incident beam, further indicating that specular reflection does not occur.

5.3 HARD-CUBE MODEL

A model for the gas-surface interaction has been proposed by Stickney⁽²⁾ which has proved useful in describing the lobular-type spatial distributions presented in Sections 4.2 and 4.3. The model assumes that the gas molecules behave as hard spheres and the solid atoms as hard cubes. The collision process is assumed elastic with the tangential component of velocity unchanged. Using such a classical mechanics approach, accounting for the distribution of speeds in the incident beam and assuming a one-dimensional Maxwellian distribution for the motion of surface atoms, the theory gives an expression for the distribution of scattered flux which agrees with experimental results.

The theory predicts the following qualitative features for lobular scattering:

Let θ'_r = angular position of lobe maximum and

$\Delta\theta = \theta_i - \theta'_r$ which gives deviation from specular angle.

- (1) θ'_r decreases and $\Delta\theta$ increases with increasing surface temperature.
- (2) θ'_r and $\Delta\theta$ both increase with increasing angle of incidence.
- (3) θ'_r decreases and $\Delta\theta$ increases with increasing gas molecular weight.

All of these features agree with the experimental results shown previously in Figures 4.2.2(b) and 4.3.1 as well as with the results of Hinchey and Foley⁽⁸⁾. The latter results also provide agreement with predictions for the effects of incident gas temperature.

These features may be explained to some extent on a physical basis. (1) At high target temperatures, the surface atoms have more energy to "push" the gas molecules away in a direction normal to the surface. (2) As the angle of incidence is increased, the incident tangential momentum also increases which tends to increase the probability of specular reflection. However, due to the smaller incident normal momentum, the surface atoms may transfer more normal momentum for larger incident angles. These two effects are somewhat offsetting with the latter seemingly taking predominance. (3) Heavier incident gas molecules are able to absorb more momentum and energy and therefore are "pushed" away from the surface more easily.

Although the qualitative features of lobular type scattering for experimental results agree well with the hard-cube predictions, no numerical comparisons have been made here, since the mass ratios μ used for the present investigation ($\mu = 0.48$ for $N_2 \rightarrow Ni$ and $\mu = 0.68$ for $A \rightarrow Ni$) exceed the limit for which the hard-cube model is expected to be valid. For large

mass ratios, multiple collisions probably occur which are not taken into account by the theory.

Predictions for the speed distribution of scattered particles are given by Logan, et al. ⁽¹³⁾ for an incident beam with a Maxwellian speed distribution and by Stickney, et al. ⁽¹⁴⁾ for a monoenergetic incident beam. For a Maxwellian incident beam, the hard-cube theory predicts a Maxwellian distribution of speeds for the scattered particles with the corresponding temperature depending on angle of reflection. Similarly, a monoenergetic incident beam results in monoenergetic scattered particles at a given θ_r . For the present nozzle-beam experiments, the latter result should be more valid than the Maxwellian result and gives the following relation in terms of flight times:

$$t_r/t_i = \sin \theta_r / \sin \theta_i . \quad (5.4)$$

If we assume that $t_r = t_m$ for purposes of comparison, then Equation (5.4) may be compared directly to the results in Section IV with t_m/t_i . For a given angle of incidence, t_m/t_i would vary as $\sin \theta_r$ reaching a value of unity at $\theta_r = \theta_i$ which is the specular angle. Examination of the data in Section IV for "clean" hot targets shows that the variations for t_m/t_i with θ_r do not follow the predictions of the theory. In general, Equation (5.4) yields values which are lower than

measured for $\theta_r < \theta_i$ and values higher than those measured for $\theta_r > \theta_i$. Use of the approach in which a Maxwellian incident beam is assumed does not improve the agreement with experimental results; however, it does allow an examination of the effects of target temperature, angle of incidence, and incident gas weight on t_m and predicts the following:

- (1) t_m/t_i decreases with increasing surface temperature.
- (2) t_m/t_i decreases with increasing angle of incidence.
- (3) t_m/t_i decreases with increasing molecular weight of incident beam.

The present results agree with all of the above predictions for the time-of-flight at maximum signal. However, the hard-cube theory does not predict the correct results for the thermal spread in the scattered beam in the monoenergetic limit, probably due to its neglect of multiple collisions.

5.4 ADDITIONAL MODELS

Nocilla's Re-emission Law - Nocilla⁽¹⁵⁾ has proposed a model for gas-surface interactions which concerns itself only with the reflected gas properties. The re-emitted particle velocity distribution is assumed to correspond to a Maxwellian superimposed on a mean velocity \vec{v}_0 and is of the form

$$f(\vec{V}) \propto \exp[-|\vec{V} - \vec{S}|^2], \quad (5.5)$$

where $\vec{V} = \beta \vec{v}$ and $\vec{S} = \beta \vec{v}_0$ in terms of previous notation. Equation (5.5) is then used to derive an expression for the re-emitted flux distribution in which S and θ_r are free parameters. (θ_r is the angle between \vec{S} and the surface normal.) These parameters may be adjusted until the derived expression for flux gives the "best" fit to a particular set of experimental data. The method provides relatively good fits for both cosine and lobular scattering patterns. However, success in fitting a given spatial distribution need not imply that the actual velocity distribution is of the assumed form. It is evident from the results of the present investigation that in general the distribution of reflected particle velocities cannot be fitted by a form as simple as that suggested by Equation (5.5).

Hinchen and Shepherd - A model similar to the hard-cube model has been proposed by Hinchen and Shepherd⁽¹⁶⁾. It uses the same assumption of no change in tangential velocity in collisions and relates the energy accommodation coefficient only to the normal component of gas velocity. For reasonably assumed values for this accommodation coefficient, this model is able to match the observed position of the lobe maximum in lobular scattering relatively well. The model is useful for describing a particular set of experimental data and yields the same predictions with regard to the speed of the reflected particles as the hard-cube theory.

"Rough-Surface" Model - While the hard-cube model explains lobular scattering as a result of thermal motion, Healy⁽¹⁷⁾ has shown that lobular scattering could still be attributed to randomly rough surfaces. His model assumes that all particles are reflected specularly from surface elements which are oriented at random. By judicious choice of a "roughness parameter" agreement with experimental results is obtained. The assumption of specular reflection is not a valid one based on the present results, since this would imply that the speed distribution of reflected particles is the same as that in the incident beam. However, the model does confirm the idea of increased dispersion of the scattered particles (i. e. , wider lobes) for an increase in surface roughness.

Other Models - Many more complicated models have been studied; however, none have been developed to an extent which allow direct comparison to the present TOF experiments. For a more complete discussion of the theoretical aspects of gas-surface interactions, the reader is referred to a summary by Trilling⁽¹⁸⁾.

SECTION VI

SUMMARY AND CONCLUSIONS

The nozzle-type molecular beam used for the present experiments is able to provide a suitably intense and nearly monoenergetic incident flux for the study of scattering of thermal energy particles from solid surfaces. Combination of a high intensity beam with a sensitive time-of-flight detection system allows accurate measurements of both the spatial and speed distributions of the scattered particles.

Experimental measurements confirm the result of cosine scattering for "dirty" targets and lobular scattering for "clean" targets. "Clean" targets have been produced by prolonged heating in a vacuum within certain temperature limits; however, present methods do not yield information as to the precise nature of surface conditions. It is probable, based on the work of Hinchey and Foley⁽⁸⁾ and Datz, et al.⁽¹⁹⁾ that adsorbed gas layers and surface crystal structure do play an important part in gas-surface interactions.

The measured variations in the position of the lobe maximum for lobular scattering agree qualitatively with the results of other researchers and the predictions of the hard-cube model for the effects of target temperature, angle of

incidence, and incident gas molecular weight.

In addition to confirming previous results, the present method has provided information about the speeds of the scattered particles and indicates the following trends:

(1) The speed distributions do not in general correspond to Maxwellian effusion and show a strong dependence of thermal accommodation on angle of reflection.

(2) The thermal spread of the reflected distributions is always smaller than that for Maxwellian effusion with full thermal accommodation and always much greater than that for the incident beam.

(3) The thermal spread decreases as the angle of incidence or reflection is increased.

It has been shown that the measured time-of-flight distributions may be fitted by analytic expressions of the form $At^{-n} \exp[-B^2(\frac{1}{t} - \frac{1}{t_0})^2]$ for the purpose of obtaining moments of the distribution. The results of an analysis of this fitting procedure indicate that the degree of fit and the magnitude of the deduced moments are relatively independent of the exponent n . The moments-mean speed and mean energy-obtained in this manner are within a few percent of those obtained by numerical integration.

Simple theories based on classical mechanics give a fairly accurate description of the spatial distribution of scattered particles; however, they are not sufficient to yield accurate

predictions for the speed distributions. More complete theoretical models are needed to explain this speed distribution behavior.

Obviously, the experimental results presented here are also far from complete. Increased knowledge and control of target surface structure, variation of incident particle energy and measurement of the full reflected spectrum (out of incident beam-surface normal plane) are areas for immediate extension of these experiments. Target surface structure changes may perhaps account for the marked qualitative change that occurs with heating of the target at or above about 1000°K.

BIBLIOGRAPHY

BIBLIOGRAPHY

1. Kaminsky, Manfred; Atomic and Ionic Impact Phenomena on Metal Surfaces, Academic Press (1965).
2. Stickney, Robert E.; "Atomic and Molecular Scattering from Solid Surfaces," to be published in Vol. III of Advances in Atomic and Molecular Physics, Academic Press (1967).
3. Scott, John E., Jr., and James E. Drewry; "Characteristics of Aerodynamic Molecular Beams," Rarefied Gas Dynamics, Vol. I, Academic Press, p. 516 (1963).
4. Hagena, Otto F., John E. Scott, Jr., and A. K. Varma; "Design and Performance of an Aerodynamic Molecular Beam and Beam-Detection System," Report AST-4038-103-67U, Research Laboratories for the Engineering Sciences, University of Virginia (1967).
5. Hagena, Otto F., "Velocity Distribution Measurements of Molecular Beams Scattered from Solid Surfaces," Applied Physics Letters, Vol. 9, No. 10, p. 385, November 1966.
6. Hurlbut, F. C., "Studies of Molecular Scattering at the Solid Surface," J. Appl. Phys., Vol. 28, p. 844 (1957).
7. Smith, Joe N., Jr., and Wade L. Fite, "Recent Investigations of Gas-Surface Interactions Using Modulated-Atomic Beam Techniques," Rarefied Gas Dynamics, Vol. I, Academic Press, p. 430 (1963).
8. Hinchey, John J., and William M. Foley, "Scattering of Molecular Beams by Metallic Surfaces," Rarefied Gas Dynamics, Vol. II, Academic Press, p. 505 (1966).
9. Hinchey, John J., and E. S. Malloy, "Velocity of Molecular Beam Molecules Scattered by Platinum Surfaces," presented at Symposium on Fundamentals of Gas-Surface Interactions, San Diego, December 1966.

10. Moran, James P., Harold Y. Wachman, and Leon Trilling, "Time of Flight Measurements in a Molecular Beam Deflected by a Heated Platinum Target," presented at Symposium on Fundamentals of Gas-Surface Interactions, San Diego, December 1966.
11. Clausing, P., Ann. Physik., Vol. 4, p. 533 (1930).
12. Knudsen, M., Kinetic Theory of Gases, Methuen and Co. Ltd., London (1934).
13. Logan, R. M., J. C. Keck, and R. E. Stickney, "Simple Classical Model for the Scattering of Gas Atoms from a Solid Surface: Additional Analyses and Comparisons," Rarefied Gas Dynamics, Vol. I, Academic Press, p. 49 (1967).
14. Stickney, R. E., R. M. Logan, S. Yamamoto, and J. C. Keck, "Simple Classical Model for the Scattering of Gas Atoms from a Solid Surface: III. Analyses for Monoenergetic Beams and for Lock-in Detector Signals," presented at Symposium on Fundamentals of Gas-Surface Interactions, San Diego, December 1966.
15. Nocilla, Silvio, "The Surface Re-Emission Law in Free Molecule Flow," Rarefied Gas Dynamics, Vol. I, Academic Press, p. 327 (1963).
16. Hinchey, John J., and E. F. Shepherd, "Molecular Beam Scattering from Surfaces of Various Metals," Rarefied Gas Dynamics, Vol. I, Academic Press, p. 239 (1967).
17. Healy, T., "The Scattering of Particles from Random Rough Surfaces," presented at Symposium on Fundamentals of Gas-Surface Interactions, San Diego, December 1966.
18. Trilling, Leon, "Theory of Gas Surface Interaction," presented at Symposium on Fundamentals of Gas-Surface Interactions, San Diego, December 1966.

19. Datz, Sheldon, George E. Moore, and Ellison H. Taylor, "The Reflection of Modulated Helium and Deuterium Molecular Beams from Platinum Surfaces," Rarefied Gas Dynamics, Vol. I, Academic Press, p. 347 (1963).
20. Hagen, Otto F., and W. Henkes, "Investigation of the Thermal Relaxation in Nozzle Flows by Analysis of the Gas Kinetic Velocity Distribution," Zeitschrift für Naturforschung, Vol. 15a, 10, p. 851 (1960).
21. Kuhlthau, A. R., and M. N. Bishara, "On the Nature of the Surface Interaction between Inert Gas Molecules and Engineering Surfaces," Rarefied Gas Dynamics, Vol. II, Academic Press, p. 518 (1966).

APPENDIX

APPENDIX

CURVE FITTING VS. NUMERICAL INTEGRATION

A. 1 DERIVATION OF MOMENTS FROM FITTED CURVE

It has been shown by Hagen and Henkes⁽²⁰⁾ for $n = 3$, generalized here for arbitrary n , that a TOF distribution of the form

$$S_d(t) = \frac{A}{t^n} \exp[-\beta^2 L^2 (\frac{1}{t} - \frac{1}{t_o})^2] \quad (A. 1)$$

may be fitted to a given experimental curve by the following procedure. Using the relations $S_d(t_1) = S_d(t_2) = \frac{1}{2} S_d(t_m)$ yields

$$\beta = t_m / L \sqrt{g(a)} \quad (A. 2)$$

and

$$\frac{L}{t_o} = \frac{L}{t_m} \cdot h(a) \quad (A. 3)$$

where $a = t_m/t_1$ or t_m/t_2 and

$$h(a) = 1 - \frac{n}{2} g(a) \quad (A. 4)$$

$$g(a) = (a - 1)^2 / [\ln 2 + n(\ln a - a + 1)]. \quad (A. 5)$$

Combining (A. 2) and (A. 3) and letting $S = \beta L/t_o$,

$$S^2 = h^2(a)/g(a). \quad (\text{A. 6})$$

Now, $S(t_m/t_1)$ and $S(t_m/t_2)$ may be combined to give $S(t_2/t_1)$. Then for given experimental values of t_2/t_1 and t_1 or t_2 , the values for S and t_m necessary to fit (A. 1) at t_1 and t_2 can be found. The constant A is determined by requiring that $S_d(t_m)$ from (A. 1) equals $S_d(t_m)$ from the experimental curve.

To find the moments of the fitted curve, it is convenient to transform (A. 1) into velocity space and express it in terms of a speed distribution function. This yields

$$dI/dv = A' v^{n-1} \exp[-\beta^2(v - v_o)^2]. \quad (\text{A. 7})$$

The mean speed is then given by

$$\bar{v} = \frac{\int_0^{\infty} v \frac{dI}{dv} dv}{\int_0^{\infty} \frac{dI}{dv} dv} \quad (\text{A. 8})$$

and the mean square speed is

$$\bar{v}^2 = \frac{\int_0^{\infty} v^2 \frac{dI}{dv} dv}{\int_0^{\infty} \frac{dI}{dv} dv}. \quad (\text{A. 9})$$

Expressions for $\beta \bar{v}$ and $\beta^2 \bar{v}^2$ have been evaluated from (A. 8) and (A. 9) for $n=3, 4$ and 5 and are given below.

$n = 3$:

$$\beta \bar{v} = \frac{\frac{1}{2} (1+S^2) e^{-S^2} + \frac{\sqrt{\pi}}{2} S \left(\frac{3}{2} + S^2 \right) (1 + \operatorname{erf} S)}{\frac{1}{2} S e^{-S^2} + \frac{\sqrt{\pi}}{2} \left(\frac{1}{2} + S^2 \right) (1 + \operatorname{erf} S)} \quad (\text{A. 10})$$

$$\beta^2 \bar{v}^2 = \frac{\frac{1}{2} \left(\frac{5}{2} S + S^3 \right) e^{-S^2} + \frac{\sqrt{\pi}}{2} \left(\frac{3}{4} + 3S^2 + S^4 \right) (1 + \operatorname{erf} S)}{\frac{1}{2} S e^{-S^2} + \frac{\sqrt{\pi}}{2} \left(\frac{1}{2} + S^2 \right) (1 + \operatorname{erf} S)} \quad (\text{A. 11})$$

$n = 4$:

$$\beta \bar{v} = \frac{\frac{1}{2} \left(\frac{5}{2} S + S^3 \right) e^{-S^2} + \frac{\sqrt{\pi}}{2} \left(\frac{3}{4} + 3S^2 + S^4 \right) (1 + \operatorname{erf} S)}{\frac{1}{2} (1 + S^2) e^{-S^2} + \frac{\sqrt{\pi}}{2} S \left(\frac{3}{2} + S^2 \right) (1 + \operatorname{erf} S)} \quad (\text{A. 12})$$

$$\beta^2 \bar{v}^2 = \frac{\left(1 + \frac{9}{4} S^2 + \frac{1}{2} S^4 \right) e^{-S^2} + \frac{\sqrt{\pi}}{2} \left(\frac{15}{4} S + 5S^3 + S^5 \right) (1 + \operatorname{erf} S)}{\frac{1}{2} (1 + S^2) e^{-S^2} + \frac{\sqrt{\pi}}{2} S \left(\frac{3}{2} + S^2 \right) (1 + \operatorname{erf} S)} \quad (\text{A. 13})$$

$n = 5$:

$$\beta \bar{v} = \frac{\left(1 + \frac{9}{4} S^2 + \frac{1}{2} S^4 \right) e^{-S^2} + \frac{\sqrt{\pi}}{2} \left(\frac{15}{4} S + 5S^3 + S^5 \right) (1 + \operatorname{erf} S)}{\frac{1}{2} \left(\frac{5}{2} S + S^3 \right) e^{-S^2} + \frac{\sqrt{\pi}}{2} \left(\frac{3}{4} + 3S^2 + S^4 \right) (1 + \operatorname{erf} S)} \quad (\text{A. 14})$$

$$\beta^2 \bar{v}^2 = \frac{\left(\frac{33}{8} S + \frac{7}{2} S^3 + \frac{1}{2} S^5 \right) e^{-S^2} + \frac{\sqrt{\pi}}{2} \left(\frac{15}{8} + \frac{45}{4} S^2 + \frac{15}{2} S^4 + S^6 \right) (1 + \operatorname{erf} S)}{\frac{1}{2} \left(\frac{5}{2} S + S^3 \right) e^{-S^2} + \frac{\sqrt{\pi}}{2} \left(\frac{3}{4} + 3S^2 + S^4 \right) (1 + \operatorname{erf} S)} \quad (\text{A. 15})$$

For convenience in obtaining the desired moments for given values of t_2/t_1 and t_1 or t_2 , the normalized quantities $\bar{v}t_m/L$ and $\bar{v}^2 t_m^2/L^2$, which are functions only of t_2/t_1 , are given in Figure A. 1.

A. 2 APPLICATION TO SAMPLE SET OF DATA

Values for \bar{v} and \bar{v}^2 have been evaluated using the method of curve fitting from Section A. 1 and by numerical integration using the relations (3. 3) and (3. 4) from Section III for several typical TOF distributions. A sample set of TOF distributions for nitrogen scattered from a hot target are shown in Figure A. 2. The signal $S_d(t)$ has been normalized with respect to $S_d(t_m)$ and the time-of-flights to t^* . A comparison of the fitted curve with an experimental curve for $\theta_r = 60^\circ$ is given in Figure A. 3. The solid and dashed lines represent Equation (A. 1) for $n = 3$ and $n = 5$ respectively. It is seen that both values of n give reasonably good fits over most of the TOF range with the $n = 5$ curve being slightly better in the range $t_1 < t < t_2$.

Moments \bar{v} and \bar{v}^2 have been calculated for this sample set of TOF distributions by numerical integration as well as from curves fitted at t_1 and t_2 . The derived moments are presented in Figure A. 4 as functions of θ_r . The quantity \bar{v} has been normalized with respect to \bar{v}_s and \bar{v}^2 to \bar{v}_s^2 where $\bar{v}_s = 3\sqrt{\pi}/4\beta_s$ and

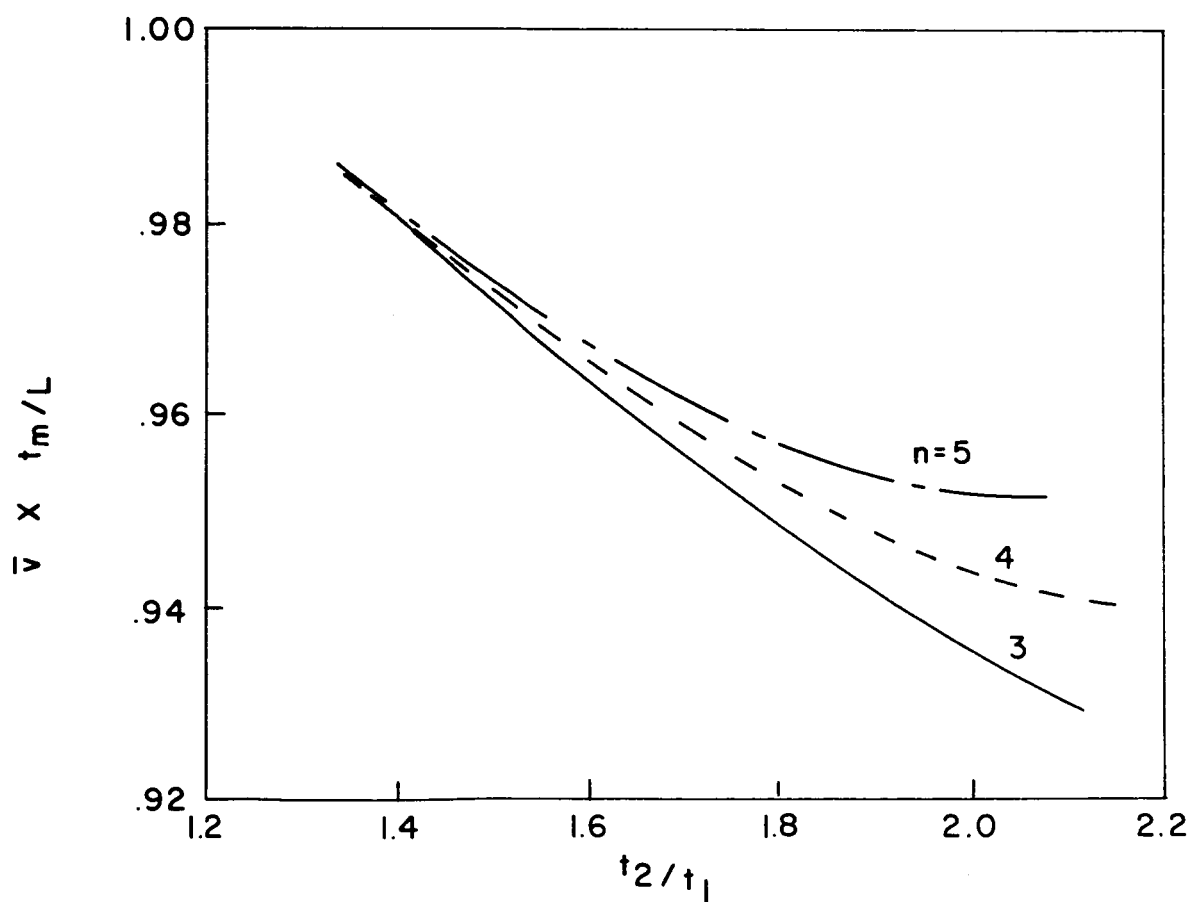
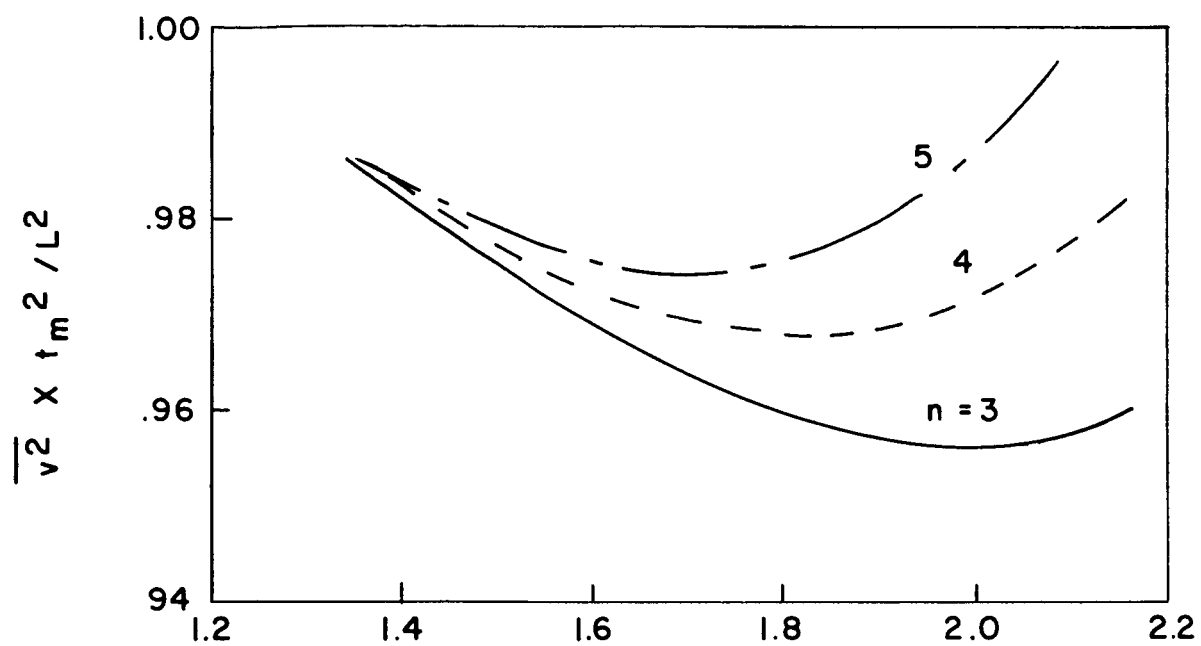


Figure A.1 Working Curves for \bar{v} and \bar{v}^2

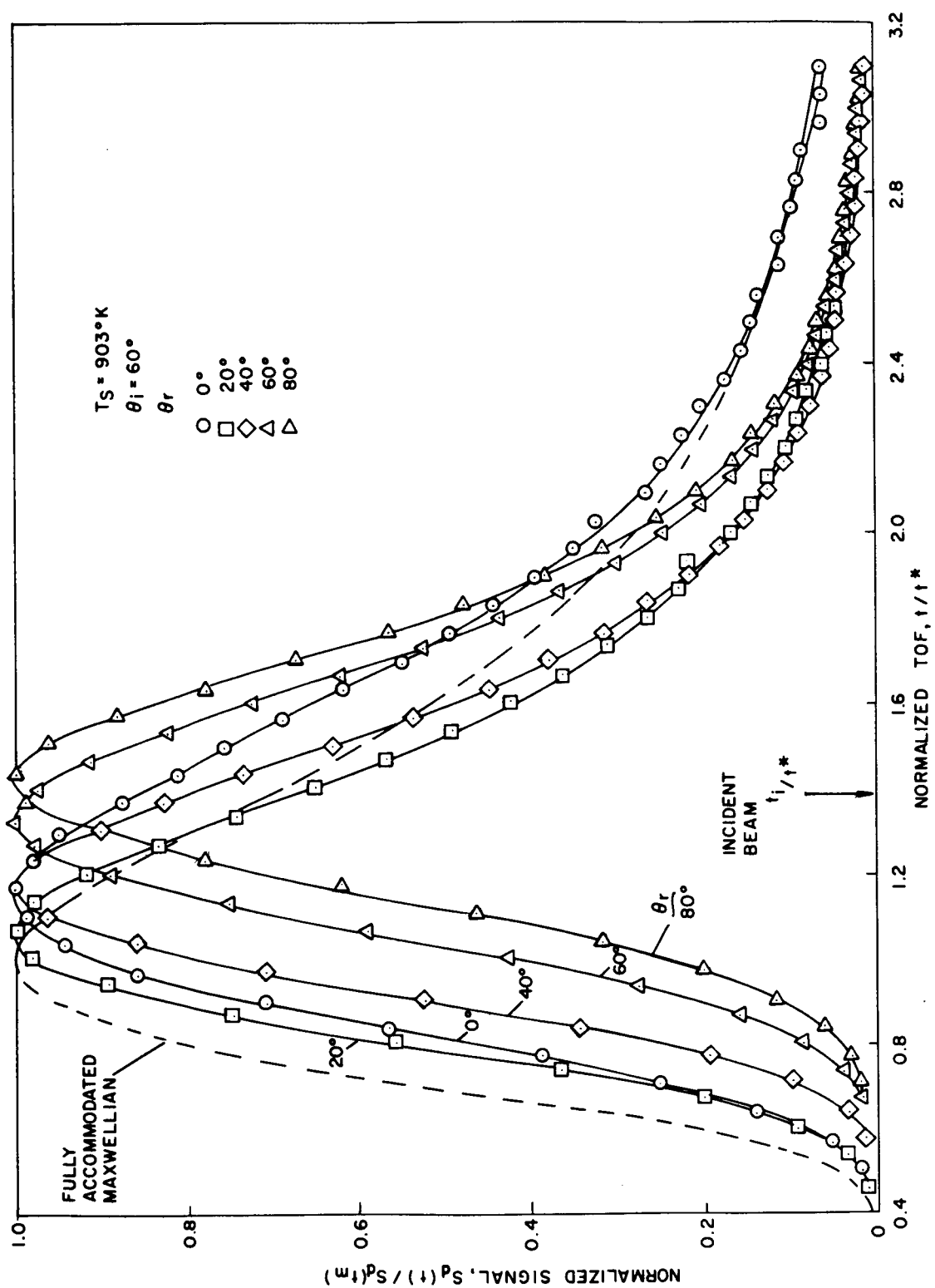


Figure A.2 TOF Distributions for Nitrogen Scattered from Hot Nickel

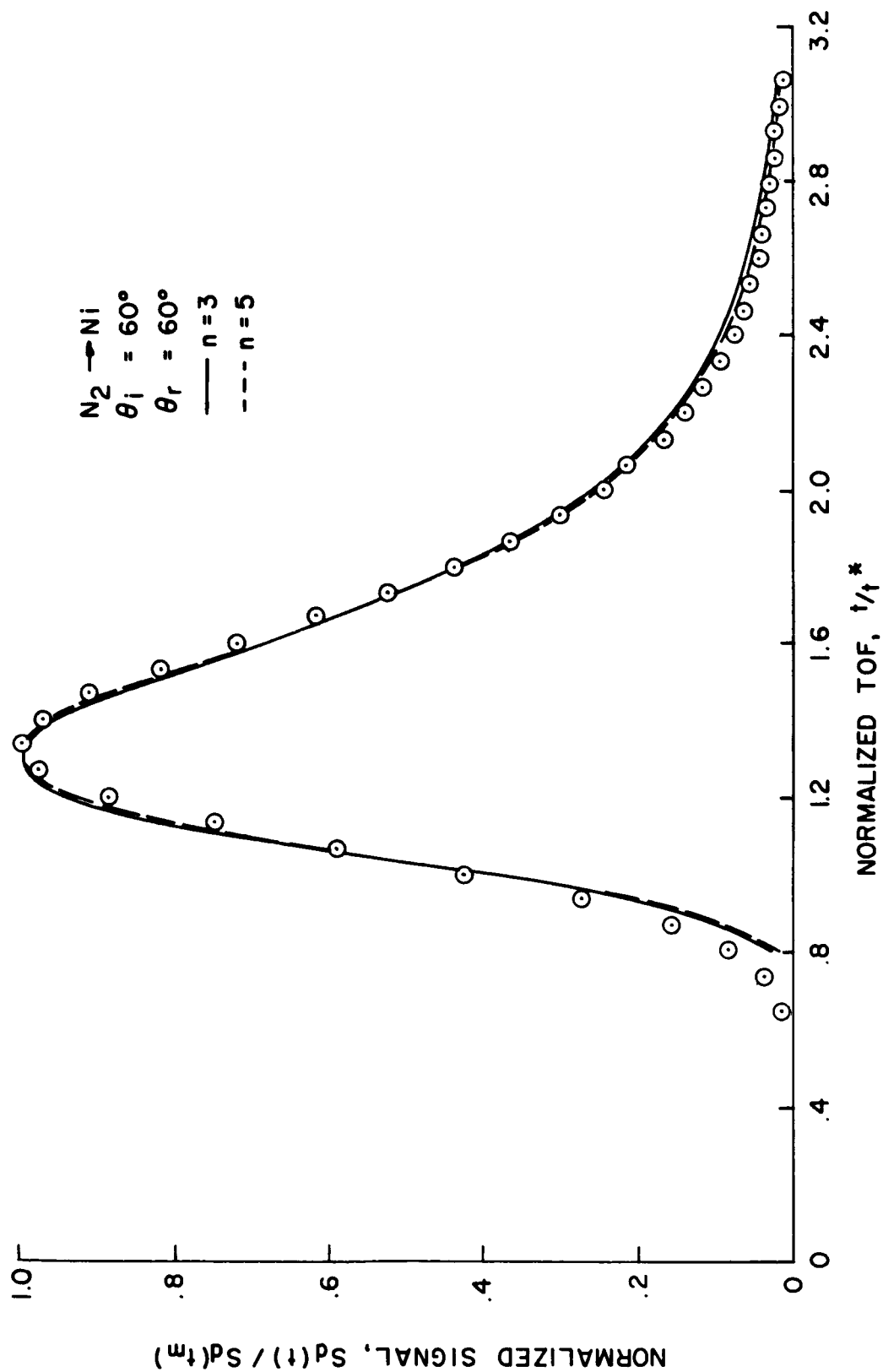


Figure A.3 Comparison of Measured and Fitted TOF Distributions

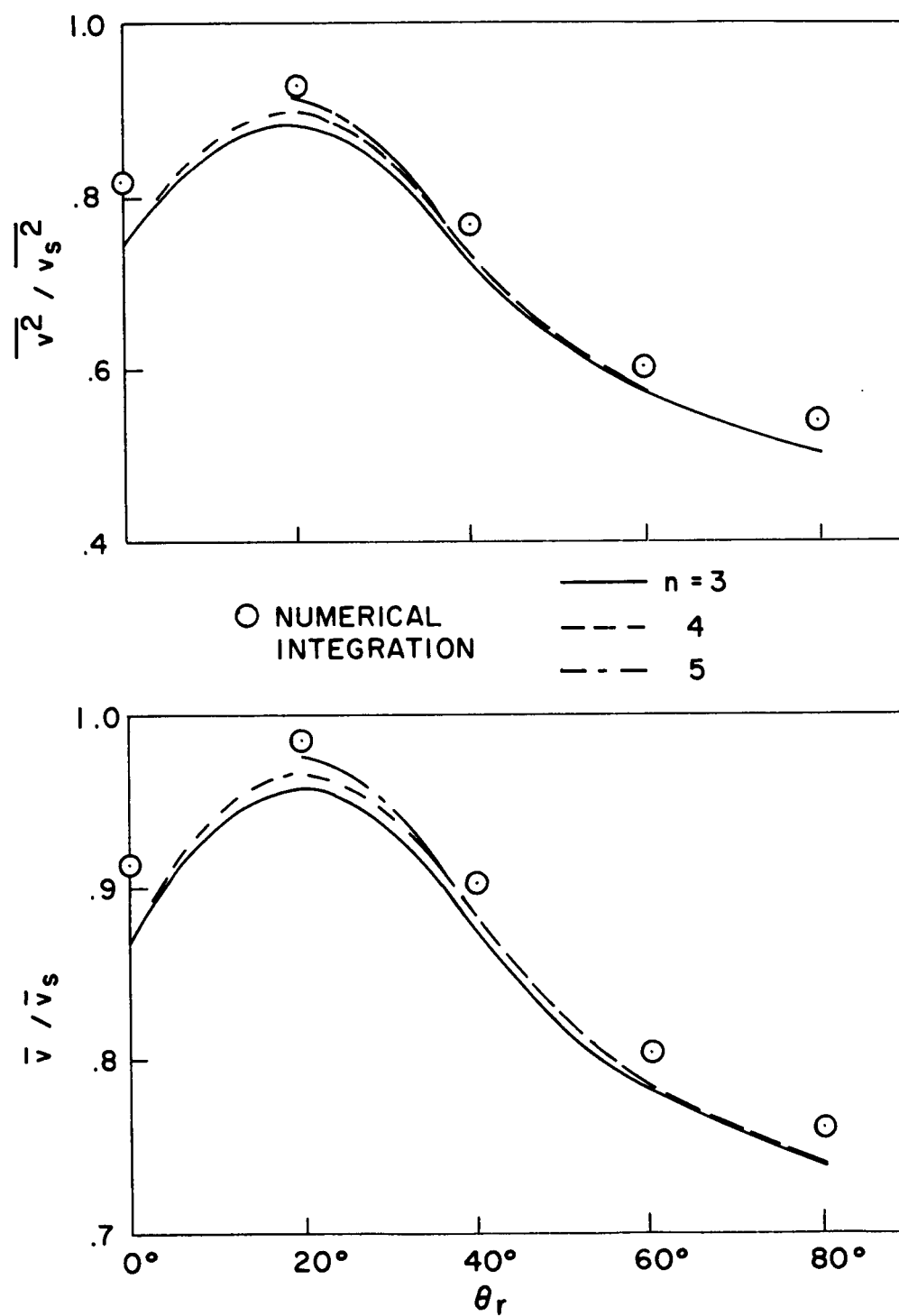


Figure A. 4

Comparison of Moments by Numerical
Integration and by Curve-Fit Method

$\bar{v}_s^2 = 2/\beta_s^2$ are the mean speed and mean square speed respectively corresponding to fully accommodated thermal effusion. The values obtained from fitting are less than those from numerical integration. This would be expected due to the higher degree of symmetry of the measured TOF distributions. However, the moments are relatively insensitive to the exponent n for these data, with $n = 5$ only slightly better. (At $\theta_r = 0^\circ$ the value of t_2/t_1 was too large to allow use of the given functional form with $n = 5$.) All values from fitted curves agree to within about 5% of those from numerical integration. These results show that the curve-fit method may be used to obtain reasonable approximations of mean momentum and energy of reflected particles.

A.3 EFFECT OF RESOLUTION

The error, due to insufficient resolution of the TOF recordings, in the deduction of these two moments can be estimated using the curve-fit method and the correction to the half-width Δt given by Hagena, et al. ⁽⁴⁾ Since the proper method for applying the correction $\Delta t - \Delta t_0$ to the measured half-width for insufficient resolution is subject to question, the following two methods will be compared:

- (1) $t_{10} = t_1 + (\Delta t - \Delta t_0)$, $t_{20} = t_2$ and
- (2) $t_{10} = t_1$, $t_{20} = t_2 - (\Delta t - \Delta t_0)$,

where quantities with subscript 0 refer to conditions for $R \rightarrow \infty$ and those without subscript 0 refer to measured quantities at resolution R . The results for a symmetrical application of the correction (i. e., $t_{10} = t_1 + \frac{1}{2} (\Delta t - \Delta t_0)$, $t_{20} = t_2 - \frac{1}{2} (\Delta t - \Delta t_0)$) should lie between these two methods. Therefore, for given measured values of t_1 and t_2 and the resolution R , the ideal values t_{10} and t_{20} may be found, since $\Delta t - \Delta t_0$ is a function of R . The corrected moments may then be evaluated using the curve-fit method for the new ratio t_{20}/t_{10} . However, due to the questionability of using either method (1) or (2) for correcting t_1 and t_2 , the method may be used only to provide upper and lower limits for the ideal moments.

Using the values of t_1 and t_2 measured for the TOF curve from Figure A. 2 for $\theta_r = 60^\circ$ and the method just outlined, ideal values for the moments \bar{v}_0 and \bar{v}_0^2 have been calculated assuming different values of R correspond to t_1 and t_2 . These curves are presented in Figure A. 5. Both quantities are normalized with respect to their uncorrected values (those assuming $R \rightarrow \infty$). The lower limit represents method (1) and the upper limit method (2) for applying the correction. It is seen that in the range of R used for most of the present experiments ($4 < R < 5$), the quantities \bar{v} and \bar{v}^2 would not be in error by more than about 3%. It should be noted that these results are merely an estimate of the error limits

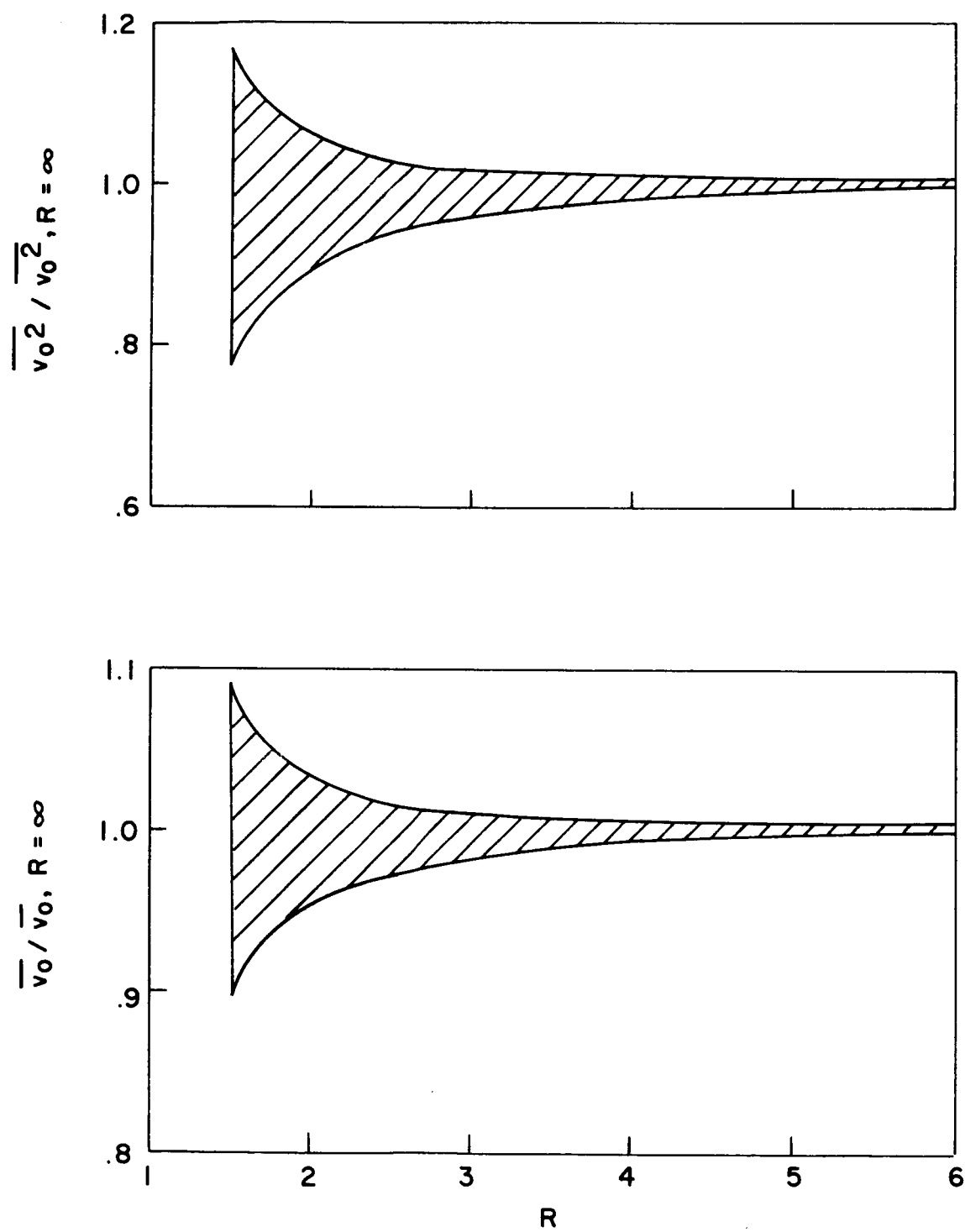


Figure A.5 Effect of Resolution on \overline{v} and $\overline{v^2}$

and that an exact analysis would require inversion of the type of integral given by Hagen, et al. ⁽⁴⁾ to find the true TOF distribution.

DISTRIBUTION LIST

Copy No.

1 - 10	Office of Grants and Research Contracts National Aeronautics and Space Administration Washington, D. C. 20546 Attention: Code SC
11	Mr. Alfred Gessow NASA Headquarters Code RRP Washington, D. C. 20546
12 - 16	O. F. Hagen Kernforschungszenrum Karlsruhe 75 Karlsruhe Postfach 947, Germany
17	A. K. Varma Department of Aerospace and Mechanical Science Forrestal Research Center Princeton University Princeton, New Jersey
18 - 19	E. L. Knuth UCLA, Department of Engineering Los Angeles, California 90024
20	Leon Trilling Department of Aerospace Engineering Massachusetts Institute of Technology Cambridge, Massachusetts 02139
21	Manuel Curtis Code 734 Goddard Space Flight Center Greenbelt, Maryland
22	F. Hushfar Optical Physics Laboratory Air Force Cambridge Research Laboratories Hanscom Field Bedford, Massachusetts 01730

Copy No.

- 23 N. Cabrera
University of Virginia
- 24 W. D. Whitehead
University of Virginia
- 25 L. B. Thomas
University of Missouri
Columbia, Missouri
- 26 K. R. Lawless
University of Virginia
- 27 F. O. Goodman
University of Sydney
School of Physics
Sydney, N. S. W., Australia
- 28 F. C. Hurlbut
University of California
Division of Aerospace Science
Berkeley, California
- 29 J. H. McGinn
General Electric Company
Valley Forge, Pennsylvania
- 30 H. Saltsburg
General Atomic
P. O. Box 608
San Diego, California 92112
- 31 J. N. Smith, Jr.
General Atomic
P. O. Box 608
San Diego, California 92112
- 32 - 33 W. M. Foley
United Aircraft Research Laboratories
East Hartford, Connecticut 06108
- 34 - 35 J. B. Fenn
Princeton University
Engineering Quadrangle
Princeton, New Jersey

Copy No.

- 36 R. E. Stickney
Department of Mechanical Engineering
Massachusetts Institute of Technology
Cambridge, Massachusetts 02139
- 37 R. A. Oman
Grumman Aircraft Engineering Corporation
Research Department
Bethpage, New York
- 38 J. B. French
University of Toronto, UTIAS
Toronto, Ontario, Canada
- 39 P. B. Scott
Department of Aerospace Engineering
Massachusetts Institute of Technology
Cambridge, Massachusetts 02139
- 40 J. C. Keck
Department of Mechanical Engineering
Massachusetts Institute of Technology
Cambridge, Massachusetts 02139
- 41 T. Healy
University of Santa Clara
Santa Clara, California
- 42 D. Menzel
Eduard-Zintl-Institut der Technischen Hochschule
Darmstadt, Germany
- 43 G. A. McAlpine
University of Virginia
- 44 - 53 S. S. Fisher
University of Virginia
- 54 J. A. Phipps
University of Virginia
- 55 H. S. Morton
University of Virginia

Copy No.

56	R. N. Zapata University of Virginia
57	M. Bishara University of Virginia
58	G. Magnuson University of Virginia
59	J. W. Boring University of Virginia
60	Office of the Provost Attention: Associate Provost for Research University of Virginia
61 - 62	University Library
63	F. M. Devienne Laboratoire Méditerranéen de Recherches Thermodynamiques 2, Ave Villebois-Mareuil 06 Nice, France
64	J. H. Heald, Jr. ARO, Inc. Arnold Air Force Station Tennessee
65	J. A. Alcalay Aerospace Corporation El Segundo, California
66	G. H. Miller Sandia Corporation Albuquerque, New Mexico
67	Milton Rogers Department of the Air Force Office of Aerospace Research (RRMK) 1400 Wilson Boulevard Arlington, Virginia 22209

Copy No.

68 - 73

J. E. Scott, Jr.
ONR Branch Office
Box 39, FPO
New York 09510

74 - 79

RLES Files

80 - 105

S. S. Fisher
University of Virginia